

Vacuum structure and string tension in Yang-Mills dimeron ensembles

Falk Zimmermann^{1,2}, Hilmar Forkel¹ and Michael Müller-Preußker¹

¹*Institut für Physik, Humboldt-Universität zu Berlin, D-12489 Berlin, Germany and*

²*HISKP and Bethe Center for Theoretical Physics, Universität Bonn, D-53115 Bonn, Germany*

We numerically simulate ensembles of SU(2) Yang-Mills dimeron solutions with a statistical weight determined by the classical action and perform a comprehensive analysis of their properties as a function of the bare coupling. In particular, we examine the extent to which these ensembles and their classical gauge interactions capture topological and confinement properties of the Yang-Mills vacuum. This also allows us to put the classic picture of meron-induced quark confinement, with the confinement-deconfinement transition triggered by dimeron dissociation, to stringent tests. In the first part of our analysis we study spacial, topological-charge and color correlations at the level of both the dimerons and their meron constituents. At small to moderate couplings, the dependence of the interactions between the dimerons on their relative color orientations is found to generate a strong attraction (repulsion) between nearest neighbors of opposite (equal) topological charge. Hence the emerging short- to mid-range order in the gauge-field configurations screens topological charges. With increasing coupling this order weakens rapidly, however, in part because the dimerons gradually dissociate into their less localized meron constituents. Monitoring confinement properties by evaluating Wilson-loop expectation values, we find the growing disorder due to the long-range tails of these progressively liberated merons to generate a finite and (with the coupling) increasing string tension. The short-distance behavior of the static quark-antiquark potential, on the other hand, is dominated by small, “instanton-like” dimerons. String tension, action density and topological susceptibility of the dimeron ensembles in the physical coupling region turn out to be of the order of standard values. Hence the above results demonstrate without reliance on weak-coupling or low-density approximations that the dissociating dimeron component in the Yang-Mills vacuum can indeed produce a meron-populated confining phase. The density of coexisting, hardly dissociated and thus instanton-like dimerons seems to remain large enough, on the other hand, to reproduce much of the additional phenomenology successfully accounted for by non-confining instanton vacuum models. Hence dimeron ensembles should provide an efficient basis for a rather complete description of the Yang-Mills vacuum.

I. INTRODUCTION

The notorious complexity of the Yang-Mills vacuum manifests itself in emergent infrared phenomena which, despite vigorous theoretical efforts over the last decades, remain only fragmentarily understood. Quark confinement [1] was early recognized as a paradigm for these infrared complexities, both because of its unprecedented nature and of its almost universal impact on the hadronic world. The long struggle to explain the nonperturbative confinement mechanism has led to the development and often ongoing refinement of a wide variety of theoretical approaches [2], ranging from various vacuum models to ab-initio lattice simulations [3]. The latter, in particular, have provided strong and unbiased evidence for the main signatures of quark confinement, i.e. the linear growth (and saturation) of the static quark-antiquark potential at large distances and the associated color flux-tube formation [4] (and breaking [5]).

Beyond establishing confinement and its characteristics, intense efforts were devoted to pinning down the underlying dynamical mechanism and to identify the infrared degrees of freedom best suited to describe it in humanly fathomable terms. Vacuum model analyses have played a prominent and often pioneering role in this endeavor. The majority of them is based on ensembles of specific “constituent” fields, i.e. at least partly localized gauge fields (with their prospective monopole loop and center vortex content) which are supposed to populate and disorder the Yang-Mills vacuum. Potential candidates for these building blocks can be classified according to the increasing number of spacetime dimensions in which they are localized, and thus equivalently to their increasing efficiency in disordering the vacuum. The minimally, i.e. in just two dimensions localized candidates are center vortices [6, 7]. An intermediate position occupy both (gauge-projected) Abelian [8, 9] and non-Abelian monopoles or dyons [10, 11] (possibly in the guise of BPS constituents [12] of KvBLL calorons [13], see below) which are localized in the three spacial dimensions.

Among the maximally, i.e. in all four (Euclidean) spacetime dimensions localized candidates for the building blocks of confining field configurations, finally, are regular-gauge instantons [14], calorons with nontrivial [13, 15–17] holonomy and merons [14, 18, 19]. All of these “pseudoparticles” carry a nontrivial topological charge, mediate vacuum tunneling events and solve the classical Yang-Mills equation [65]. The latter property, in particular, has raised hopes that at least one of these solutions may provide a basis for semiclassical and therefore potentially analytical treatments of confinement. (This proved indeed possible in lower-dimensional models where instantons or vortices were shown to generate confinement at weak coupling [21, 22].) In classically scale-invariant, four-dimensional Yang-Mills

theory, however, where one is inevitably faced with large couplings at large distances, the justification for semiclassical approximations depends crucially on the characteristic distance scales involved. A successful semiclassical description of confinement, in particular, would require all physically relevant confinement effects (as, for example, the quark binding inside light hadrons) to take place over distances which remain small enough to avoid the strong-coupling regime.

In order to overcome these potentially stymying limitations, one may resort to simulating fully interacting pseudoparticle ensembles numerically. The first and still most extensive such calculations were based on rather dilute superpositions of instantons and anti-instantons in singular gauge [23]. Such superpositions maintain part of the instantons' semiclassical nature, are known to generate a variety of important physical effects including spontaneous chiral symmetry breaking, and describe a large amount of successful vacuum and hadron phenomenology [23]. However, they fail to generate a confining, i.e. linearly growing potential between static quarks [24–26]. By now, numerical simulations were performed for superpositions of all the other above-mentioned pseudoparticle candidates as well. A central result was that each of them proved capable of generating a finite string tension.

The discovery of new finite-temperature instantons [13] has given renewed impetus to semiclassically inspired confinement models. These generalized calorons contain N_c self-dual monopole (“dyon”) constituents without classical interactions and carry a non-trivial holonomy as an explicit degree of freedom. The ability of the calorons to separate into N_c quasi-independent constituents (without cost in action) in the confinement phase has led to simulations [17] where the separation appears as an additional (internal) degree of freedom compared to the “old-fashioned” instanton simulations. Encouraging results have been obtained. Later, an analytic solution for the caloron-dyon gas was proposed [12] at the price of a non-positive weight of an overwhelming multitude of configurations with respect to the moduli metric [27]. An analytic as well as numerical treatment of the purely Abelian non-interacting dyon gas was shown to provide a confining force [28].

In addition, equilibrated lattice gauge-field configurations were successfully searched for the presence of pseudoparticles (with the notable exception of merons) in the Yang-Mills vacuum. Such searches are typically performed by smoothing techniques designed to filter out infrared gluon fields and in particular solutions of the classical Yang-Mills equation. For examples in the most extensively studied case of instantons and their size distribution see Refs. [29], and for calorons with nontrivial holonomy Refs. [16].

In the present paper, building upon the above developments, we are going to introduce and study a new type of pseudoparticle ensemble. The latter is based on superpositions of dimers and anti-dimers (in singular gauge), i.e. on those four-dimensionally localized solutions of the classical $SU(2)$ Yang-Mills equation which contain two meron centers [18]. The relatively large dimeron solution family includes as one extreme members which are contracted to (singular-gauge) instantons and as another members which are dissociated into two far separated merons. Moreover, it contains continuous sets of dimeron fields which interpolate between these extremes. Hence our configuration space includes many of the previously studied singular-gauge instanton and single-meron configurations and is ideally suited to study transitions between instanton and meron ensembles. This is a crucial advantage because such a transition process was conjectured to take place between the instanton, dimeron and meron components of the Yang-Mills vacuum as a function of the bare gauge coupling. Indeed, this transition is a central ingredient of the meron-induced confinement scenario which was put forward on the basis of qualitative arguments by Callan, Dashen and Gross (CDG) [24, 30] (and further explored in several promising directions, including e.g. a two-phase picture of hadron structure [31] which received some support from lattice simulations [32]). (For more recent work on merons see Refs. [33]. An alternative meron confinement mechanism was suggested in Refs. [34].)

The CDG confinement scenario was inspired by the already mentioned weak-coupling confinement mechanism in 2+1 dimensional Yang-Mills-Higgs theory [21, 22]. In contrast to this classic paradigm, however, even the ingenious use of semiclassical arguments turned out to be of limited use in 3+1 dimensional Yang-Mills theory. In fact, the resulting estimates remained qualitative at best [66]. Further progress was achieved only recently, when a numerical study of superpositions of merons and antimeron [14, 19] provided the first convincing support for a central assumption of the CDG scenario, namely that the meron component of the Yang-Mills vacuum may indeed confine, i.e. generate a static quark potential which rises linearly at large interquark separations. The suggested origin of the meron population in the vacuum from dimeron dissociation remained obscure, on the other hand, since the field content was from the outset restricted to a purely meronic phase.

To search for the development of such a meron-dominated phase and to analyze the underlying mechanism in dimeron-antidimeron ensembles evolving under the Yang-Mills dynamics will therefore be important points on our agenda. For this purpose, and in contrast to previous simulations of pseudoparticle ensembles, we will monitor pertinent vacuum properties in a wide range of gauge coupling values. In particular, we will look for signatures of the envisioned dimeron dissociation process. Similar to the gradual break-up of molecules into their atomic constituents with increasing temperature, this dissociation is suggested to be driven by a competition between the decreasing attraction among the dimeron's regularized meron centers and the entropy [67] gain from their increasingly distant positions. Guided by the behavior of an ideal dimeron gas, one may indeed roughly estimate the inter-meron attraction

to decrease relative to the entropy with growing coupling. In view of the strong interactions anticipated especially between the meron centers of different dimers in significantly dissociated ensembles, however, such estimates are unreliable. Moreover, in our dynamical context the coupling-dependent competition between energy and entropy is particularly subtle since both attraction and entropy are expected to depend only logarithmically on the intermeron separation [68]. This further impedes even qualitative analytical estimates of dimeron ensemble properties.

Our fully interacting ensembles, on the other hand, are well suited to tackle and clarify these issues. Since they take all classical gauge interactions – including those which may be strong, long-range or many-body – between the dimers into account, we do not have to rely on the semiclassical or any other weak-coupling or low-density approximation. Nevertheless, it will be of heuristic value and of help for future, possibly more analytic treatments to understand which aspects of the dimeron-ensemble dynamics may be described semiclassically. In fact, one of our reasons for transforming the individual dimers into a singular gauge was to provide additional insight into this issue by more strongly localizing them. This allows the dimers and their meron centers to retain their identities and their classical shapes to a larger extent, even in the presence of quantum fluctuations, and thus facilitates (semi-)classical behavior. At several points during the course of our investigation we will therefore check for indications of such behavior.

Besides studying the dimeron dissociation process and its dynamics in detail, we will also survey other structural and topological properties of the ensemble configurations. In particular, we will examine distributions and correlations of the topological charge carriers and search for ordering tendencies with respect to both dimeron and meron centers. (A side benefit for investigating topology distributions is that dimers, in contrast to e.g. center vortices and monopoles [38], carry the topological charge of the Yang-Mills gauge group [69] directly.) This will result in a more detailed understanding of the restructuring processes which accompany the transition to the strong-coupling regime. We will pay particular attention to the behavior of the topological susceptibility and of confinement properties, which we monitor by evaluating Wilson-loop expectation values and the associated string tension, as a function of the bare coupling. The quantitative picture emerging from these investigations will reveal, in particular, at which stage of dissociation (as quantified e.g. by the average separation of the dimers' meron partners) dimeron ensembles can best describe the confining phase of the Yang-Mills vacuum.

In the next section we start by acquainting the reader with pertinent properties of the dimeron solutions, transform them into a singular gauge and discuss the regularization of their singularities. We then set up our ensemble field configurations and write down their partition function. Section III presents an outline of our simulation strategy and, in particular, of the measures taken to control systematic finite-size and discretization errors. The next and central Sec. IV contains our results and their discussion. We start with an extensive statistical analysis of the spacetime, topological-charge and color structure of the ensemble configurations as well as of the crucial dimeron dissociation process. These investigations provide a broad spectrum of insights into the behavior of the dimeron ensemble and its phase structure as a function of the gauge coupling. They furthermore relate this behavior to the changes in the average properties of the individual dimers. We then evaluate the topological susceptibility and the static quark potential (based on the calculation of Wilson-loop expectation values) and analyze the results in relation to the coupling-dependent restructuring of the ensemble configurations. We further discuss scale-setting issues, evaluate dimensionless observable ratios, rewrite our results in physical units and confront them with those of other approaches. Section V, finally, contains a summary of our main findings and presents our conclusions.

II. SINGULAR-GAUGE DIMERON CONFIGURATIONS AND THEIR DYNAMICS

In the following subsections we construct the (continuum) dimeron field-configuration space on which our study will be based. Along the way, we will motivate our expectation that such dimeron configurations approximate crucial features of the gauge-field population in the Yang-Mills vacuum, and in particular that they may provide a decent description of the confinement-deconfinement transition with decreasing gauge coupling. We start by deriving the building blocks of our fields, i.e. the individual dimeron solutions of the Yang-Mills equation in singular gauge, and discuss their collective coordinates. We then superpose these solutions to define our gauge-field configuration space and write down the partition function which specifies its dynamics. Finally, we discuss the (both gauge-dependent and -independent) singularities of our configurations and introduce suitable regularization procedures to prepare for their numerical treatment in Sec. III.

A. Yang-Mills dimers in singular gauge

Dimers (or meron pairs) are those classical solutions of the Euclidean Yang-Mills equation which contain two meron centers where their only singularities are located [18]. In regular gauge, with the two merons located symmet-

rically at the distances $\pm a$ from the center at x_0 , the SU(2) dimeron solution family reads [18]

$$A_\mu^{(D,r)}(x; \{x_0, a, u\}) = \left[\frac{(x - x_0 + a)_\nu}{(x - x_0 + a)^2} + \frac{(x - x_0 - a)_\nu}{(x - x_0 - a)^2} \right] u^\dagger \sigma_{\mu\nu} u \quad (1)$$

where $\sigma_{\mu\nu} := \eta_{a\mu\nu} \sigma_a / 2$ with the Pauli matrices σ_a and the 't Hooft symbols $\eta_{a\mu\nu}$. (The latter are defined as $\eta_{a\mu\nu} = \varepsilon_{a\mu\nu}$, $\eta_{a\mu 4} = -\eta_{a4\mu} = \delta_{a\mu}$ for $\mu, \nu = 1, 2, 3$ and $\eta_{a44} = 0$ [39].) The unitary matrices u are global SU(2) color rotations. The dimerons (1) carry the same topological charge as instantons, i.e. $Q = 1$. The anti-dimeron $\bar{A}_\mu^{(D,r)}$ with opposite topological charge $Q = -1$ is obtained from Eq. (1) by replacing $\eta_{a\mu\nu} \rightarrow \bar{\eta}_{a\mu\nu} := (-1)^{\delta_{\mu 4} + \delta_{\nu 4}} \eta_{a\mu\nu}$. In contrast to instantons, however, dimerons are not selfdual.

The solution class (1) depends on eleven real and continuous ‘‘collective coordinates’’ or ‘‘moduli’’ whose values uniquely and completely specify each member. Eight of these parameters, $x_{0,\mu}$ and a_μ , determine the spacetime position and orientation of the dimeron while the remaining three determine the SU(2) group elements u [70]. The collective coordinates correspond to those eleven independent combinations of the classical and continuous Yang-Mills symmetries, i.e. of Euclidean spacetime translations and rotations, conformal transformations and global SU(2) color rotations, which transform a representative dimeron into a gauge-inequivalent solution [40].

It is instructive to consider several limits of the solution family (1). For $a \rightarrow 0$ the meron centers coalesce and the dimeron turns into a pointlike, regular-gauge instanton. (A finite-size instanton is reached after suitably regularizing the meron singularities, cf. Sec. II C.) For $|a| \rightarrow \infty$, on the other hand, the dimeron breaks up into two merons. Although these merons maintain the fixed relative color orientation of Eq. (1), changing it by hand will yield increasingly action-degenerate two-meron solutions when the inter-meron separation $|a|$ becomes large. This is because the color-dependent attraction which locks the meron constituents of Eq. (1) into their rigid color orientation decreases with increasing $|a|$. Hence both instantons and merons are contained in the solution class (1) as limiting cases. The fields (1) therefore provide on-shell interpolations between instantons and isolated meron pairs, i.e. continuous paths in Yang-Mills solution space which connect these particular gauge fields. In our context these paths are of particular interest since they provide preferred doorways along which the dimerons may dissociate into merons. As already mentioned, such dissociation processes are conjectured to drive the deconfinement-confinement transition.

The solutions (1) have the same $|x| \rightarrow \infty$ behavior as an instanton in regular gauge [35, 41, 42], i.e. they contain a long-distance tail

$$A_\mu^{(D,r)}(x) \xrightarrow{|x| \rightarrow \infty} 2 \frac{x_\rho}{x^2} \sigma_{\mu\rho} \quad (2)$$

$\sim 1/|x|$ which implies an exceptionally weak localization. In multi-dimeron configurations these tails generate strong overlap interactions between the individual dimerons. Building dimeron ensembles by superposing solutions of the type (1) would thus lead to very strongly correlated systems, in some respects similar to the regular-gauge instanton ensembles studied in Ref. [14]. In the present work we will take a different route, however. In contrast to merons, dimerons – like instantons – may be transformed to singular gauges in which they are more strongly localized, with their long-range tails decaying as $1/|x|^3$. A superposition of singular-gauge dimerons thus improves the vacuum description at short distances, compared to superpositions of either regular-gauge instantons or single merons. As long as the characteristic dimeron size is small compared to the average inter-dimeron separation, furthermore, it will provide much better approximations to classical Yang-Mills solutions. This is essentially because at moderate pseudoparticle densities the contribution of the overlap regions to the action is much smaller than in regular-gauge dimeron superpositions. Hence singular-gauge multi-dimeron configurations provide a privileged testing ground especially for the semiclassical features of the CDG confinement mechanism [24, 30, 31].

In addition, dimeron configurations in singular gauge may also describe less classical or even fully quantum-mechanical aspects of confinement. This holds, in particular, for the vacuum disordering mechanism envisioned by CDG. The latter relies on the long-distance tails of the individual merons which come into play when the separation $|a|$ between the meron centers of the dimerons becomes large. As discussed above, the partner merons are then practically independent and regain their long-range tail $\sim 1/|x|$ (at least in isolation). The ensuing long-distance color correlations among these merons were found in Refs. [14, 19] to be far from semi-classical and to generate confinement. Of course, a complete dimeron dissociation into isolated and thus far separated merons is impossible in the finite spacetime volumes in which numerical simulations are feasible. (The same holds for the solution in which one of the merons delocalizes on the three-sphere at spacetime infinity [18, 24].) However, such isolated merons would anyhow be unphysical (since they carry infinite action) and incompatible with a finite dimeron density. Instead, one expects that beyond some typical separation the two meron centers of a dimeron experience stronger interactions with their individual field environment than with their partner. The rigid link between their color orientations can then be broken, i.e. the partner merons can become effectively independent of each other.

In order to construct the multi-dimeron configurations motivated above, we first transform the dimeron solution family (1) into a specific singular gauge,

$$A_\mu^{(\text{D},\text{s})} = \hat{U}^\dagger(\hat{x}) A_\mu^{(\text{D},\text{r})} \hat{U}(\hat{x}) + i\hat{U}^\dagger(\hat{x}) \partial_\mu \hat{U}(\hat{x}), \quad (3)$$

where \hat{U} is the large, i.e. topologically active gauge group element

$$\hat{U}(\hat{x}) = i\hat{x}_\mu \sigma_\mu^{(+)} \quad (4)$$

($\sigma_\mu^{(+)} \equiv (\vec{\sigma}, -i)$, $\hat{x}_\mu \equiv x_\mu/\sqrt{x_\nu x_\nu}$) which has a singularity at the origin of the coordinate system. The result can be cast into the form

$$A_\mu^{(\text{D},\text{s})} = f_1(x, a) x_\nu \bar{\sigma}_{\mu\nu} + f_2(x, a) a_\nu X_{\mu\nu}(\hat{x}) \quad (5)$$

($\bar{\sigma}_{\mu\nu} := \bar{\eta}_{\alpha\mu\nu} \sigma_\alpha/2$). Choosing for simplicity $x_0 = 0$ and $u = 1$, the two scalar functions $f_{1,2}$ become

$$f_1(x, a) := \frac{2}{x^2} - \frac{1}{(x+a)^2} - \frac{1}{(x-a)^2}, \quad (6)$$

$$f_2(x, a) := \frac{1}{(x+a)^2} - \frac{1}{(x-a)^2}. \quad (7)$$

The antisymmetric and anti-selfdual field $X_{\mu\nu}$ contains important parts of the SU(2) and spacetime tensor structures (and their mutual couplings). Explicitly,

$$X_{\mu\nu}(\hat{x}) = \eta_{\alpha\mu\nu} X_\alpha(\hat{x}) \quad \text{with} \quad X_a(\hat{x}) = \left(\frac{1}{2} - \hat{x}_r \hat{x}_r\right) \sigma_a + \hat{x}_a \hat{x}_s \sigma_s - \hat{x}_4 \hat{x}_s \varepsilon_{asc} \sigma_c \quad (8)$$

(latin indices are spacial). After regularization of the short-distance singularity (cf. Sec. II C) the $a \rightarrow 0$ limit turns the dimeron (5) into a singular-gauge instanton with $f_1(x, a=0) = 2\rho^2/[x^2(x^2 + \rho^2)]$ and $f_2(x, a=0) = 0$. In the following, we will often refer with the term ‘‘dimeron’’ to both dimerons and anti-dimerons in singular gauge. Occasionally, we will use the term ‘‘pseudoparticle’’ for the same purpose.

The leading asymptotic behavior of the singular-gauge dimerons (5) is

$$A_\mu^{(\text{D},\text{s})} \xrightarrow{|x| \gg |a|} -4 \frac{a_\rho x_\rho}{x^4} a_\nu \eta_{\alpha\mu\nu} X_\alpha(\hat{x}) \sim \frac{1}{x^3}, \quad (9)$$

i.e. the long-range tail (2) has as intended disappeared and the overlap between neighboring dimerons is strongly reduced. (This is in contrast to the meron ensembles of Refs. [14, 19] whose constituents exist only in regular gauge.) In addition to the meron-center singularities at $x = \pm a$, the solution (5) inherits another singularity at $x = 0$ from the gauge transformation (4). Hence the impact of the latter will disappear when forming (topologically insensitive) gauge-invariant quantities from Eq. (5). The regularization of these singularities will be discussed in Sec. II C.

By construction, the singular-gauge dimerons (5) provide only a subset of the full solution family. The complete eleven-parameter family can be recovered by translating the solutions (5) to x_0 and by gauge-rotating them with a constant matrix $u \in \text{SU}(2)$, i.e.

$$A_\mu(x; \{x_0, a, u\}) = u^\dagger A_\mu^{(\text{D},\text{s})}(x - x_0) u = R_{ab}(u) A_\mu^{(\text{D},\text{s}),b}(x - x_0) \frac{\sigma_a}{2} \quad (10)$$

where the orthogonal matrices $R_{ab}(u) = \text{tr} \{ \sigma_a u^\dagger \sigma_b u \} / 2$ are obtained from the condition $u^\dagger \sigma_b u = R_{ab}(u) \sigma_a$. The group elements u depend on three real and continuous parameters which form (local) coordinates on the SU(2) group manifold S^3 . In the following it will be convenient to use the quaternion representation

$$u(c) = c_0 + i c_a \sigma_a \quad (11)$$

which embeds S^3 into R^4 with Euclidean coordinates c_0, \dots, c_3 by imposing the unit three-sphere constraint $\sum_{\alpha=0}^3 c_\alpha^2 = 1$. In these coordinates R takes the form

$$R_{ab}(u(c)) = (c_0^2 - c_c c_c) \delta_{ab} + 2c_a c_b - 2\varepsilon_{abc} c_0 c_c. \quad (12)$$

For our discussion below it will be useful to keep in mind that dimerons have three more continuous and noncompact collective coordinates than instantons (but three less than a pair of independent merons, due to the locking of the inter-meron color orientation). The three additional coordinates arise from the more complex structure of extended (i.e. $|a| \neq 0$) dimerons which requires more degrees of freedom to locate and orient them in spacetime. This results in a substantially larger ‘‘position entropy’’ [24, 43] which is instrumental in counterbalancing the (regularized) dimeron action which grows logarithmically with $|a|$. Indeed, the larger entropy is a necessary (but not sufficient) requirement for dimerons to dissociate with increasing coupling g^2 and to finally split up into their meron partners.

B. Field configurations and partition function of the dimeron ensembles

As motivated above, we intend to study a model which drastically reduces the field content of Yang-Mills theory (as integrated over in amplitudes and the partition function) to superpositions of N_D dimerons and $N_{\bar{D}} \simeq N_D$ antidimerons in singular gauge [71], i.e.

$$A_\mu(x, \{C_{I,i}, \bar{C}_{\bar{I},i}\}) = \sum_I^{N_D} A_\mu^{(D,s)}(x; \{C_{I,i}\}) + \sum_{\bar{I}}^{N_{\bar{D}}} \bar{A}_\mu^{(D,s)}(x; \{\bar{C}_{\bar{I},i}\}) \quad (13)$$

with $N \equiv N_D + N_{\bar{D}}$. Each term in this sum is uniquely characterized by the set $\{C_I\} = \{x_{0,I}, a_I, c_I\}$ of collective coordinates of the corresponding (anti-) dimeron. We recall that the configurations (13) differ distinctly from those obtained by transforming a regular-gauge dimeron superposition into (any) singular gauge. This is because in Eq. (13) the gauge of each dimeron is chosen relative to its individual position. One may wonder, incidentally, whether n -meron solutions with $Q > 1$ and their anti-solutions should be added to the superposition ansatz (13). As in the case of instantons, however, the Bogomoln'yi-type bound $S \geq (8\pi^2/g^2) |Q|$ on the action [41] implies that such multi-(anti)-meron contributions to the partition function are exponentially suppressed relative to the dimeron contributions [72]. Since the entropy increases only logarithmically with n and thus cannot compensate this suppression, such multi-meron contributions may be safely neglected.

Nevertheless, the ansatz (13) should be regarded as a rather minimal choice. It is mainly geared towards a transparent study of the proposed (instanton and) dimeron dissociation mechanism and its role in the deconfinement-confinement transition [24, 30, 31]. Hence there are several natural directions in which Eq. (13) may be extended in future studies to provide a more complete description of the Yang-Mills vacuum physics. An example would be to add the meron-antimeron pair solutions [18] of the Yang-Mills equations, again individually transformed into singular gauge. This would maintain the approximately semiclassical nature of the configurations at small $|a|$ and yield a richer dynamics. However, it would probably also lead to a less transparent interpretation of the results, and we do not expect the topologically trivial meron-antimeron pair configurations to provide qualitatively new insights into the transition behavior. Indeed, their limits for $|a| \rightarrow 0$, a pure-gauge field of zero action, and for $|a| \rightarrow \infty$, a meron and an independent antimeron, indicate that meron-antimeron pairs do not generate new pathways for the transition. More promising improvement options would include generalizations of the dimeron superposition ansatz (13) which allow for a complete transition into a meron ensemble (e.g. by releasing the rigid color locking between the dimerons' meron partners beyond a suitable intermeron separation $|a|_{\min}$) or the admixture of a pure instanton component [24, 31] with a realistic size distribution [44].

As discussed above, we view the dimeron configurations (13) as a pertinent subset of the SU(2) gauge fields governed by the Yang-Mills dynamics. Hence we define the partition function of our dimeron model as

$$Z = \int \prod_{I, \bar{I}}^{N_D, N_{\bar{D}}} dC_I d\bar{C}_{\bar{I}} \exp \left\{ -S [A_\mu (\{C_{I,i}, \bar{C}_{\bar{I},j}\})] \right\} \quad (14)$$

where S is the Euclidean Yang-Mills action

$$S[A] = \frac{1}{2g^2} \int d^4x \text{tr} \{F_{\mu\nu} F_{\mu\nu}\} =: \int d^4x s(x) \quad (15)$$

and $F_{\mu\nu}$ is the gauge field strength

$$F_{\mu\nu}(x) = \partial_\mu A_\nu(x) - \partial_\nu A_\mu(x) - i[A_\mu(x), A_\nu(x)]. \quad (16)$$

As already indicated, we expect the gauge interactions among the dimerons in Eq. (14) to play an important role in generating confining long-range correlations for large $|a|$ and, in particular, to provide a disordering mechanism for the vacuum. This is in contrast to the situation in non-confining singular-gauge instanton ensembles where for most amplitudes a random orientation of the instantons (i.e. the neglect of the interaction term $\exp(-S)$ in Eq. (14)) yields a reasonable approximation to the vacuum physics [23].

The integration over the collective coordinates will be performed with the measure

$$dC = d^4x_0 d^4a d\mu(\vec{c}) \quad (17)$$

($d\mu(\vec{c})$ is the SU(2) Haar measure) for the dimerons, and analogously for the anti-dimerons. This type of measure is familiar from instanton vacuum models [23]. An improved alternative may include Jacobians which arise from the transformation of the linear gauge-field measure dA into the collective-coordinate basis and thereby implement the full moduli-space metric. Finally, an additional a dependence of the measure can emerge from the trace anomaly [24, 31].

C. Regularization of the gauge-field singularities

The singular-gauge dimeron solutions (5) contain two types of singularities. The first are those located at the constituent meron centers $x = x_0 \pm a$ which persist in any gauge. In addition, there is a gauge singularity inherited from the topologically large and thus necessarily singular gauge transformation (4), chosen to sit at the origin. In isolated dimerons, such gauge singularities could be gauged away and would therefore not affect (topologically insensitive) observables. This ceases to be the case for the superpositions (13), however, where the location of the gauge singularities varies with the positions of the pseudoparticles.

Since both types of singularities would impede our numerical simulations, they have to be regularized in a physically acceptable manner. (Recall that the individual dimeron fields (1) and (5) do not solve the Yang-Mills equation at their singularities, so that a suitably localized regulator will only minimally affect the semiclassical properties of the configurations (13).) A natural way to regularize the singularities at the meron centers is to add the square of a “size” parameter ρ to the denominators $(x - x_0 \pm a)^2$ in Eqs. (6) and (7). Such a regulator imitates the way in which the size parameter enters the instanton solutions. Hence it may arise from scale-symmetry breaking quantum fluctuations which are expected to smear the classical singularities. A finite ρ furthermore acts as a UV cutoff since it limits the gradients of the configurations (13). Of course, the regularized field configurations cease to be exact solutions of the classical Yang-Mills equation. Hence the value of ρ should be chosen large enough to avoid sizeable discretization errors (cf. Sec. III D) but also small enough to avoid unnecessary deformations of the dimeron solutions from the semiclassical saddle points. We have found $\rho^2 = 0.3$ to be a reasonable compromise between both criteria and will use this value in our numerical simulations, if not stated otherwise.

The remaining singularities are, at least for isolated dimerons, gauge artefacts. They remain unlikely to have a physical impact in our dimeron superpositions, too, but they may nevertheless cause problems in numerical approximations (even for single dimerons), e.g. when subtle cancellations in gauge-invariant quantities are upset by discretization errors. A finite-size regulator as above would hardly help to avoid such problems since it would just spread out the unphysical action-density peaks at the singularities. Hence we treat these gauge-dependent singularities in a pragmatic way, namely by interpolating the gauge field in $4d$ balls of radius ε around the singularities with the field value at a specific point on the surface of the ball. In practice, it turns out that with $\rho^2 = 0.3$ these highly localized singularities are smoothly regularized by taking ε as small as $\varepsilon = 5 \times 10^{-10}$. (The values of dimensionful quantities, such as ρ and ε above, are given in “numerical units” originating from the discretization grid to be introduced in Sec. III A. As a convenient length unit we have chosen $a = 0.1$, i.e. a tenth of the distance between nearest grid points. (Of course, this a should not be confused with the four-vector a which parametrizes the dimeron solutions.) When transforming our results into physical units starting from Sec. IV C, we will denote quantities in these numerical units by a hat above their symbols, cf. Sec. IV C.) In our simulations it typically took several hundred sweeps through configurations of $N = 487$ pseudoparticles (cf. Sec. III B) before such a singularity was first encountered. (Even with a dramatically reduced floating-point variable length of 16 bits, incidentally, we have observed no overflows (which unregularized gauge singularities would generate) when evaluating the action density of a regularized two-dimeron configuration.)

III. SIMULATION DETAILS

In the following subsections we summarize how we have generated the dimeron configuration ensembles on which all our subsequent calculations will be based. We further discuss predominant sources of systematic errors in these ensembles.

A. Sampling volume and resolution

Owing to the translational invariance of the Yang-Mills dynamics (15), ensemble averages over the pseudoparticle configurations (13) in infinite spacetime will likewise be translationally invariant. In our simulations we are restricted to a bounded volume of numerically manageable size, on the other hand, and thus have to keep boundary artefacts in calculated amplitudes under control, ideally within the size of the statistical uncertainties. Our initial step in this direction was to adopt *singular-gauge* dimerons with their more rapidly decaying long-range tails as the constituents of our gauge-field configurations (13). A sufficient suppression of boundary artefacts turned out to require additional measures, however, since the overlap among the still rather moderately localized dimerons generate important (and typically repulsive) interactions over ranges beyond the average nearest-neighbor distance. In fact, these interactions are expected to play an important role in the confinement mechanism and should thus be distorted as little as possible

by the boundary. Simulation costs, on the other hand, with their by far largest part due to integrating the action density on a spacetime grid, should be kept minimal.

In order to approximately meet these conflicting goals, we will adopt a multi-layered description of the boundary with decreasing grid-point density towards the outer layers, as sketched in Fig. 1. The innermost “core volume” is a rectangular spacetime box in which we intend to evaluate amplitudes and thus require the physics to best approximate the infinite-volume limit. In order to allow for an efficient evaluation of Wilson loops with elongated time directions in Sec. IV F, this volume and its grid are chosen to be asymmetric. One dimension, singled out as the Euclidean time direction, contains 40 grid points while each spacial dimension contains 25. This turns out to provide a sufficiently high resolution for the amplitudes to be calculated below (cf. Sec. III D).

The core volume is encompassed by an “ensemble volume” which contains the (anti-) meron centers of all (anti-) dimers. Its surface is implemented numerically by rejecting Metropolis updates (cf. Sec. III B) during which a meron center would leave this volume. The extent of the ensemble volume in a given direction will be taken 15% larger than that of the core in the same direction. In the part of the ensemble box which surrounds the core we reduce the grid-point density to $(2/3)^4 \sim 20\%$ of that in the core volume. This turns out to yield a still adequate resolution while substantially reducing the computational cost of evaluating the action.

A satisfactory suppression of field distortions inside the core volume turns out to require an additional precautionary measure, however. It consists in correcting for a particularly prominent boundary effect, namely the artificial attraction of the pseudoparticles to the surface of the ensemble volume. The latter arises because a substantial part of the action density of dimers near the boundary is located outside the ensemble volume and thus not accounted for while the compensating tails of outside dimers reaching into the ensemble volume are neglected. We approximately remove this artefact by surrounding the ensemble box with another, “covering” volume which extends beyond the ensemble box by 10% of the core size in each direction. To keep the additional computational costs under control, we decrease the grid-point density of the outermost shell (i.e. the part of the covering volume not shared by the ensemble volume) inversely with the distance from the ensemble boundary. Since this shell does not contain the rapidly varying fields close to the meron centers, calculating the action in the full covering volume indeed largely prevents the fake attraction to the ensemble boundary (cf. Sec. IV B). Alternatively, finite-size effects in pseudoparticle ensembles can be efficiently corrected by employing the Ewald summation technique, as has been shown very recently in the simpler case of Abelian dyon field ensembles [28].

B. Monte-Carlo updates with dynamical resolution and step-size adaptation

We evaluate the discretized functional integral over the pseudoparticle fields, i.e. the multi-dimensional integral over their collective coordinates in the partition function (14) or any other amplitude, stochastically by Monte-Carlo importance sampling. Hence we average over dimeron configurations chosen randomly from a Gibbs distribution with Boltzmann factor $\exp(-S)$ where S is the Yang-Mills action (15). More specifically, we use the Metropolis algorithm to generate homogeneous Markov sequences of dimeron configurations that visit fields with larger probabilities more often. After reaching equilibrium, the probability of finding a configuration in the ensemble of subsequently generated fields follows the Gibbs distribution.

The initial pseudoparticle configurations for these Markov sequences are obtained by choosing their collective coordinates from a uniform random distribution. This procedure has equal access to all members of the configuration space and practically always results in configurations far from equilibrium, with actions several orders of magnitude above their equilibrium values. We have also tested various more ordered initial arrangements of the dimers and convinced ourselves that those lead within errors to equivalent equilibrium ensembles (see Sec. III D).

For the Markov update of the n -th configuration A_n to its sequel A_{n+1} according to the Metropolis rules, we first generate some candidate configuration A' by randomly choosing an individual pseudoparticle in A_n and modifying alternately (from one candidate to the next) either its position, i.e. $a_\mu \rightarrow a_\mu + da_\mu$ and $x_{0,\mu} \rightarrow x_{0,\mu} + dx_{0,\mu}$, or its color orientation $c_i \rightarrow c_i + d\mu(c_i)$. The increments da , dx_0 and dc are chosen randomly and uniformly subject to the constraint that their length remains limited. More specifically, we demand $|dx_0| \in [0, |dx_0|_{\max}]$, $|da| \in [0, |da|_{\max}]$ as well as $|dc| \in [0, |dc|_{\max}]$ [73] and further restrict $|da|_{\max} = |dx_0|_{\max}$. The candidate configuration A' is accepted as the new configuration A_{n+1} with probability $\min\{1, \exp(S[A] - S[A'])\}$. If a candidate is rejected, the unchanged configuration is taken as A_{n+1} (and included in measurements like all others).

The choice of the maximal modification step sizes $|da|_{\max}$ and $|dc|_{\max}$ can be used to optimize both the thermalization rate and the decorrelation among subsequent field configurations of the generated ensembles. This requires a compromise between too small values, which impede the progression through configuration space, and too large values which more strongly decorrelate subsequent configurations but cause an unefficiently large update rejection rate. Examination of the relation between maximal step sizes and typical acceptance probabilities suggests an optimal acceptance rate of about 25% for updates in both position and color space. During the initial thermalization process

we will therefore increase (decrease) the maximal step sizes $|da|_{\max}$ and $|dc|_{\max}$ after every 10 consecutive candidate field configurations by 10% if the average acceptance rate for these configurations falls below (rises above) 25%.

This dynamical step-size adaptation procedure accelerates the approach to equilibrium and avoids getting trapped into approximate would-be equilibria. Initially, i.e. far from equilibrium and near the high-action random configurations, the fields can relax in larger steps while closer to equilibrium the action fluctuations become smaller and require decreasing step sizes to maintain sufficient acceptance rates. From the time when approximate equilibration sets in, however, the step size is kept constant to preserve detailed balance. We further note that increasing g increases the acceptance probability since the Yang-Mills action (15) scales as g^{-2} . Hence larger g allow for larger step sizes, accelerate thermalization (in less Markov steps) by decreasing the autocorrelation time and result in equilibrium ensembles with larger entropy.

As a case in point, for $g^2 = 1$ (and $\rho^2 = 0.3$) we find $|da|_{\max} \sim 0.05$ and $|dc|_{\max} \sim 0.1$ in equilibrium, where the scale of the fluctuations is set by the competition between action and entropy. (For $\rho^2 = 0.2$, i.e. for more strongly localized meron centers, one instead reads off the smaller values $|da|_{\max} \sim 0.025$ and $|dc|_{\max} \sim 0.2$ from Fig. 2.) For $g^2 = 10^2$, on the other hand, one finds the indeed substantially larger maximal step sizes $|da|_{\max} \sim |dc|_{\max} \sim 0.5$ (again for $\rho^2 = 0.3$). The decreasing step width during a typical thermalization history is plotted in the uppermost row of Fig. 2 for $g^2 = 1$ and $g^2 = 25$. Note that different step sizes in position and color space are generally required to obtain action changes of comparable magnitude.

The efficiency of the ensemble generation process can be further improved by exploiting the during equilibration decreasing ruggedness and action of the dimeron configurations in yet another way, namely by starting on coarser grids and increasing the resolution only when a higher accuracy of the action evaluation becomes necessary. Indeed, as long as the action density is comparable to or larger than its value around the regularized meron centers, a reduced resolution is generally sufficient and can save computer time. During thermalization the overall action decreases strongly, however, and the grid must be refined to prevent the then more prominent meron centers from artificially reducing their action density by “hiding” between grid points. In practice, we implement this refinement procedure by starting the simulations with a $(1/3)^4$ times smaller grid-point density. When the values of suitable quantities (e.g. the distance between nearest-neighbor meron centers) begin to saturate, this factor is increased to $(2/3)^4$. Only after again reaching approximate saturation the full grid-point density of Sec. III A is activated for the final approach to equilibrium and the subsequent generation of the thermal ensembles. The approximate saturation plateaus and subsequent grid refinements (indicated by dotted vertical lines) are clearly visible in the thermalization histories of Fig. 2.

In the following we will denote a set of $2N$ consecutive Markov steps as a “sweep” (where $N = N_D + N_{\bar{D}}$, cf. Sec. II B). During such sweeps each pseudoparticle of a configuration is on average once considered for a full update. (The factor two arises since the individual Markov steps attempt to modify either a dimeron’s position or its color orientation, i.e. only one of the two subsets of its degrees of freedom.) After four consecutive sweeps with the acceptance rate kept fixed at $1/4$, all pseudoparticles in a configuration are therefore on average updated once. In order to reduce autocorrelations among ensemble configurations and thus to increase the statistical independence of successive measurements, we will only select the configurations generated by every fifth sweep (after approximate equilibration of the Markov chain) as ensemble members and employ a binning procedure to calculate amplitudes and their errors (cf. Sec. III E).

C. Approach to equilibrium

As indicated in the previous section, a reliable calculation of vacuum expectation values as ensemble averages requires a sufficient thermalization of the Markov sequences which generate the ensemble configurations. Our criteria for when their distribution approximates the equilibrium distribution closely enough are based on the measurement of several observables and correlations to be described below.

First insights into the configurations’ thermalization properties can be gained by following the Markov evolution of the average distance \bar{d} of a fixed meron center to its nearest neighbor as a function of the number of sweeps. Two examples for such histories are depicted in the second row of Fig. 2. In the left panel the coupling is set to $g = 1$, i.e. our smallest value, which results in the slowest equilibration rates we have to deal with in this paper (cf. Sec. III B). (For these measurements we have also selected a smaller meron-size regulator $\rho^2 = 0.2$ which further slows the equilibration process.) A first and general insight to be read off from this figure is how the degree of thermalization reached after a given number of sweeps depends on the measured quantity. While the average distance to the closest neighboring meron of equal topological charge appears to have equilibrated after about 800 sweeps, the analogous distance for oppositely charged merons may not be fully thermalized even after 1200 sweeps. A similarly long equilibration history can be observed for the average probability \bar{f} that the nearest neighbor of a given meron center has opposite topological charge, as plotted in the last row of Fig. 2. This behavior seems to indicate that the

average distance between two meron centers from the same dimeron equilibrates faster than their average separation from the meron centers of neighboring dimers. For $g^2 = 25$ the typical relaxation times reduce to at least half of those at $g^2 = 1$, confirming the expectation that more strongly coupled ensembles thermalize faster.

For a better understanding of the global thermalization behavior, and especially of the character and uniqueness of the reached equilibria, we have also compared ensembles resulting from different initial configurations. More specifically, we have prepared a set of initial dimeron arrangements in which the pseudoparticles were regularly positioned at maximal average distances. Their topological charges, color orientations and sizes were chosen either to approximate different types of action minima or to imitate close-to-equilibrium configurations found in previous thermalization runs.

All ensembles resulting from these different initializations turned out to generate within errors the same averages. This provides, for once, evidence for the ergodicity of the underlying Markov process, i.e. for its ability to access any possible dimeron configuration in a finite number of steps. More importantly, this result strongly supports the conclusion that the thermalization processes indeed have come sufficiently close to equilibrium, i.e. that our measurements in Sec. IV are performed in almost thermalized ensembles. This conclusion is strengthened by the fact that all our runs with non-random initializations were performed at $g^2 = 1$ where equilibration is particularly slow.

D. Finite-size and discretization errors

We now turn to the analysis of the systematic errors which arise from finite-resolution and finite-size effects. We then describe the steps taken to control them by accordingly refining our calculational strategy. Additional error-reduction measures, which apply to the calculation of specific amplitudes only, will be outlined in their corresponding sections below.

Discretization errors arise in our context from the practical necessity to sample the field configurations (13) on spacetime grids of finite resolution. To meet our accuracy requirements, we adapt the grid-point density according to the characteristic length and gradient scales in the pseudoparticle configurations under consideration. During thermalization, where these scales change drastically, we do so dynamically as described in Sec. III B. In the (approximately) thermalized ensembles, on the other hand, these scales are essentially fixed by the pseudoparticle density and by the size of the regularized meron-center singularities [74]. As described in Sec. II C, the regulator is chosen about five times larger than the lattice unit $a = 0.1$, at $\rho \simeq 0.55$. This proves sufficient to keep the action of an isolated dimeron practically independent of its position on the grid. Although configurations with gradients larger than those around single meron centers frequently occur among the dimeron superpositions (13), their enhanced action renders them relatively unimportant when thermalization is achieved. This explains why we did not encounter such configurations in our equilibrated ensembles (cf. Sec. IV B).

The grid resolution's impact on the calculated action values and on the thermalization process can be seen directly in the Markov evolution histories of Fig. 2. The two vertical lines indicate the sweep numbers at which the resolution of the grid is refined (cf. Sec. III B). The full resolution, corresponding to $a = 0.1$, is reached only after the second refinement step. In order to provide a particularly stringent test of discretization errors, we have reduced our regulator ρ for this simulation by a factor of four, to $\rho = 0.14$. This size is of the order of the minimal lattice unit and about half of the value $\rho \sim 0.3$ below which discretization errors become a concern. As a consequence, one observes that the evolution of both plotted quantities (i.e. the average meron-center distances $\langle d_{\text{nearestMM}} \rangle$ and the probability for the nearest neighbor-meron to have opposite $Q = \pm 1/2$) on the coarsest grid begins to saturate at a preliminary would-be equilibrium when further relaxation is prevented by insufficient action-density resolution. Already after the first grid refinement, however, relaxation continues until the deviation from the thermal values reduces to about 15 – 20%. The equilibrium values are approached after the second refinement step. For our standard meron size $\rho \simeq 0.55$ the discretization errors will of course be much smaller and should be well under control. This conclusion is confirmed by checks on other observables, e.g. when calculating link elements and their concatenations into Wilson loops in Sec. IV F.

We now turn to the discussion of finite-size effects. Those are artefacts of the simulation volume's boundary and turn out to be more difficult to control than the discretization errors. Our choice of the more strongly localized dimers in singular gauge (5) as the constituents of the configurations (13) was partly motivated by reducing such boundary effects. For the same purpose we designed the multi-layered boundary outlined in Sec. III A. Nevertheless, sizeable boundary artefacts of different origins, of different g^2 dependence and with varying impact on the calculated quantities remain to be dealt with. In order to analyze those quantitatively, we start by monitoring violations of translational invariance in the ensemble-averaged action density $\langle s(x) \rangle$ as a function of the distance from the boundary for two values of g^2 . The results are of direct physical and practical importance since $\langle s \rangle$ is related to the gluon condensate and since a reliable evaluation of the action is indispensable for generating trustworthy ensembles.

The action density $s(x)$, as defined in Eq. (15), can be obtained analytically by inserting the dimeron superposition

(13) into the field strength (16). The ensemble average $\langle s \rangle$ is then evaluated as outlined in Sec. III B, with ensemble configurations taken from every fifth sweep after equilibration. In order to visualize the local homogeneity properties of the action density in different sectors of the simulation volume, we plot $\langle s \rangle$ in Figs. 3 and 4 as a function of the distance from the center of the box along two different directions. The latter were chosen to provide insight into the anisotropy of the boundary effects, caused in particular by our asymmetric grid with its elongated temporal direction. (Instead of calculating the values of $s(x)$ at neighboring, equidistant points throughout these directions, we surround them with adjacent hypercubic boxes of side length 0.2 inside which we sample $s(x)$ at 10 randomly chosen points.)

We start our discussion of the $\langle s \rangle$ plots with those generated at our smallest coupling value, $g^2 = 1$. In the left panel of Fig. 3 we show $\langle s \rangle$ (black squares, full line) along the time direction, in the right panel along the average over all diagonals of the spacial box at the mid point of the time axis. Deviations from a translationally invariant, i.e. constant $\langle s \rangle$ near the center of the box are somewhat smaller along the time direction than along the diagonal. This is expected since the former keeps a larger distance from the spacial boundaries. Nonetheless, $\langle s \rangle$ fluctuates considerably even in the temporal direction and even close to the box center. A reasonable fit to a constant plateau remains possible inside most error bars up to distances of order 1.0 both along the time and diagonal directions, however, as also shown in Fig. 3. Beyond distances of about ten lattice units the missing field contributions from outside of the box volume (cf. Sec. III A) begin to reduce the action density substantially.

As a consequence of these results, we will restrict the volume in which we evaluate amplitudes to subvolumes of the core box in which the maximal distances from the center are of order one (if not noted otherwise). To demonstrate the g^2 dependence of the boundary effects, we further show the two analogous $\langle s \rangle$ profiles for $g^2 = 25$ in Fig. 4. Clearly, the boundary effects are strongly reduced and the regions close to the center now show manifest plateaus which extend up to distances ~ 1.5 from the center. With further increasing g^2 the boundary artefacts become even more restricted to the surface region until the growing dimeron dissociation (i.e. the growing intermeron distance $2|a|$) creates a different type of sensitivity to the boundary, as discussed in Secs. III A and IV B.

Since in general both character and strength of the boundary artefacts are amplitude dependent, we have also monitored the vacuum expectation value of quadratic “probe” Wilson loops W as a function of their distance from the box center. The results will guide us in reliably calculating the expectation values of rectangular Wilson loops in Sec. IV F. Since the largest among these loops play a crucial role in understanding the confinement properties of dimeron ensembles, it becomes especially important to understand the boundary’s impact on them. We survey it by evaluating the expectation values $\langle W \rangle$ of quadratic Wilson loops (for details see Sec. IV F) of side length 0.5 centered along the same two lines as the action density $\langle s \rangle$ above. The loop orientation turns out to have no significant impact on the value of $\langle W \rangle$ and will thus be averaged over. In Fig. 3 we have included plots of $450 \times \langle W \rangle$ along the time direction in the left panel and along the average over the spacial diagonals in the right panel for $g^2 = 1$, and in Fig. 4 we display $20 \times \langle W \rangle$ for $g^2 = 25$. In all four cases, with growing t, r the distance dependence of $\langle W \rangle$ becomes increasingly proportional to that of the average action density $\langle s \rangle$. For quadratic Wilson loops of minimal size this is expected since such “plaquettes” form the essential part of a discrete approximation to the Yang-Mills action density. In our case, the observed proportionality further indicates that the configurations are sufficiently smooth over our rather large test loops, probably because their side length is comparable to the regulated meron size $\rho \simeq 0.55$.

To summarize, while discretization errors in our dimeron simulations can be reliably controlled, we have observed significant violations of translational invariance in both action density and Wilson loops. Although our efforts to reduce boundary artefacts prove effective close to the center of the core box, substantial deviations from homogeneity set in at distances of order one, in particular for our smallest coupling value $g = 1$ where they are most pronounced. These boundary effects originate from a combination of the strong intermediate-range interactions between dimerons and the collective effects emanating from the boundary (cf. Sec. III A). The lessons learned from the above analysis will guide us in keeping boundary artefacts of our results tolerably small, mainly by relying on specifically reduced volumes in which to evaluate amplitudes.

E. Ensemble statistics

The effective dimeron field theory introduced in Sec. II has three adjustable parameters: the gauge coupling g^2 , the meron-center size ρ , and the approximately equal numbers $N_D \simeq N_{\bar{D}}$ of dimerons and antidimerons. We have generated all our ensembles with $N = N_D + N_{\bar{D}} = 487$ pseudoparticles, divided into $N_D = 243 \simeq N/2$ dimerons and $N_{\bar{D}} = 244 \simeq N/2$ antidimerons, in the multi-layered multi-grid volume specified in Sec. III A. The meron centers are smeared as described in Sec. II C, with a common regulator value $\rho^2 = 0.3$. We have generated two independent ensembles for each of the coupling values $g^2 \in \{1, 25, 100, 1000, \infty\}$ (with decreasing number of members) and a third one for $g^2 = 1$. The total number of sweeps per coupling in equilibrium as well as the maximal stepsizes are collected in Tab. I

In order to estimate autocorrelation effects in the ensembles with $g^2 = 1$, where they should be maximal, we

| g^2 | # of sweeps | $ da _{\max}$ | $ dc _{\max}$ |
|----------|-------------|---------------|---------------|
| 1 | 1843 | 0.04 | 0.11 |
| 25 | 1550 | 0.20 | 0.40 |
| 100 | 1470 | 0.36 | 0.44 |
| 1000 | 554 | 0.47 | 0.49 |
| ∞ | 574 | 0.10 | 1.00 |

TABLE I: Dimeron ensemble characteristics. (For definitions see Sec. III B.)

have calculated autocorrelation functions for several quantities of interest, including the average distance between nearest-neighbor meron centers of equal and opposite topological charges. For those of opposite topological charge the autocorrelations decay fastest, after about 300 – 400 equilibrium sweeps, while this takes up to a few hundred sweeps longer for equally charged neighbors. The autocorrelation functions for the average distance between nearest-neighbor dimerons, on the other hand, show no obvious preference for either equally or oppositely charged neighbors. Both distances approximately decorrelate after 500 sweeps. The same holds for the average distance between the dimerons' meron partners.

Based on the above observations, we have adopted the following strategy to reduce autocorrelations. The ensembles contain the configurations generated by every fifth Metropolis sweep. The total number of equilibrium sweeps (per coupling) is divided into ten bins. (For $g^2 = 1$ a bin thus contains about 180 sweeps and about 36 ensemble configurations.) The quantities of interest are then calculated on every ensemble configuration, and their mean values are obtained for each bin. Finally, the ensemble average is computed as the mean value of the bin averages, and its error is estimated as the standard deviation among the bin averages (if not noted otherwise). (On an Intel Core 2 Quad Q6700 processor at 2.67 Ghz a thermal Markov step takes about $t_m \sim 7$ seconds and a thermal sweep $2Nt_m \sim 1.89$ hours.)

IV. RESULTS AND DISCUSSION

In the following subsections we analyze the physics content of dimeron ensembles which were numerically generated at the five squared coupling values $g^2 = \{1, 25, 100, 1000, \infty\}$ according to the procedure outlined in Sec. III.

A. Dimeron dissociation as a function of the gauge coupling

One of the essential features of the CDG mechanism is that with increasing coupling instantons are supposed to gradually dissociate into dimerons and to finally break up into their two meron partners. This process is suggested to be driven by a competition between the attraction among the regularized meron centers and their position entropy which increases with g^2 (since the latter plays the role of temperature in the classical statistical analog ensemble). The competition is effective because both energy and entropy depend logarithmically on the distance $2|a|$ between the meron centers. In fact, this distance will play a key role in characterizing both the structure of the ensembles' dimeron constituents and the interactions among them. The latter depend sensitively on the dimerons' color dipole moment which is of $O(a^2)$.

Before the dimerons break up completely, they should already have effectively released their two meron centers which then become the dynamically active degrees of freedom. In fact, this is expected to signal the onset of a phase transition in a finite system like ours where a complete $|a| \rightarrow \infty$ dissociation is prevented by the boundary. With their slowly decaying and thus strongly overlapping long-distance tails ($\sim 1/x$) the essentially independent merons may then sufficiently disorder the vacuum to generate linear quark confinement. In the above sense, our dimeron configurations thus approach confining meron ensembles of the type studied in Refs. [14, 19]. One should keep in mind, however, that our dimeron superposition ansatz (13) is not rich enough to describe ensembles of completely independent merons since it does not allow to untie the rigid color locking between the meron partners.

Guided by the above considerations we are thus led to study the coupling dependence of the average dimeron dissociation $2\langle|a|\rangle$ in our ensembles. These average inter-meron distances, which contribute to the typical dimeron size scale $\sim 2(\rho + \langle|a|\rangle)$, are plotted as a function of the square coupling g^2 in Fig. 5 and listed in Table II. As expected, the average dimeron dissociation $2\langle|a|\rangle$ initially increases rather strongly with g^2 . For our two largest square couplings $g^2 = 1000$ and ∞ , on the other hand, its value approaches saturation since it becomes comparable to the linear extent of the ensemble box. Hence $2\langle|a|\rangle$ will be underestimated in this coupling region. Moreover, large

dimerons close to the boundary are then increasingly forced to align themselves with the boundaries, and the largest dimerons accumulate along the box diagonals. Below we will nevertheless find indications for the meron centers (which are color zero-poles) to gradually replace the dimerons (i.e. color dipoles) as the dynamically most relevant degrees of freedom when the coupling increases, as alluded to above.

| g^2 | $2 \langle a \rangle$ |
|----------|-------------------------|
| 1 | 0.267 ± 0.003 |
| 25 | 0.567 ± 0.001 |
| 100 | 0.893 ± 0.003 |
| 1000 | 2.239 ± 0.014 |
| ∞ | 3.061 ± 0.016 |

TABLE II: The average inter-meron distance $2 \langle |a| \rangle$ for five values of the square coupling.

B. Spacetime structure of the dimeron configurations

We begin to explore the multi-dimeron physics of our ensembles by analyzing the spacetime structure of a typical member configuration. To this end we survey the action density of this field configuration and its amount of local (anti-) selfduality on different hyperplanes of the simulation volume. More specifically, we display these quantities as two-dimensional density plots in two section planes through the core volume which are chosen parallel to the $x_4 - x_1$ plane. One of them is separated from the $x_4 - x_1$ plane by the distances $(x_2, x_3) = (0.4, 0.4)$ in the remaining directions, i.e. it lies rather close to the boundary in these transverse directions. The other one is positioned close to the center in the x_3 direction, at $(x_2, x_3) = (0.4, 1.2)$. (The origin of our coordinate system coincides with a corner of the core box. The spacial axes $x_{1,2,3}$ range from 0 to 2.5 and the x_4 axis from 0 to 4. Hence the box center is located at $(x_1, x_2, x_3, x_4) = (1.25, 1.25, 1.25, 2)$, cf. Sec. III A.)

Since the detection and control of boundary effects is a recurrent issue when dealing with dimeron ensembles, we draw all plots for a $g^2 = 1$ configuration where the impact of the boundary is maximal (at least up to $g^2 \simeq 1000$) and thus best analyzable. Such weak-coupling configurations with their small entropy are of additional interest because they are most likely to approximate semi-classical fields. In fact, at not too high densities (and not too large meron size regulators) such fields would be dominated by rather isolated and strongly contracted singular-gauge dimerons. These dilute superpositions of almost instanton-like solutions (cf. Sec. IV A) indeed approximate semiclassical systems quite similar to those studied in instanton vacuum models [23]. The following plots are designed to check how far our $g^2 = 1$ configuration resembles such semi-classical fields.

Although our numerically generated dimeron field configurations contain redundant, i.e. gauge-dependent information without impact on observables, it is of technical interest to understand their spacetime structure since they lay the foundation for all our ensuing work. We have therefore examined typical dimeron ensemble configurations on the above set of hypersurfaces and found the fields to be fairly smooth. More importantly, all prominent spacial features of the gauge fields components were found to be closely mirrored in the gauge-invariant densities to be discussed below. In particular, we have found no evidence for the build-up of gauge-dependent peaks (potentially approximating gauge singularities [45]) which could adversely affect the simulation behavior even though they are invisible in gauge-invariant quantities. Hence we can refrain from plotting selected components of the gauge field itself.

Instead, we turn to the gauge-invariant action density $s(x)$ of our example configuration which is plotted in the two mentioned planes through the core volume in the two left panels of Fig. 6. The graphs indicate that the action density is indeed rather smooth, with the exception of a few dilute peaks. All these peaks show a slightly nonspherical shape and an extension of about 0.5. Now we recall from Table II that for $g^2 = 1$ the average distance between the (anti-) meron centers of the (anti-) dimerons is $2 \langle |a| \rangle \sim 0.27$. This is about half of the regularized meron size $\rho \simeq 0.55$ and suggests to identify the peaks with the two strongly overlapping meron centers of the regularized dimerons. The average number of peaks is indeed consistent with the pseudoparticle density of the configuration. Moreover, the somewhat elongated action density of the peaks finds a natural explanation in the small but finite separation between the meron centers. Finally, in the more central $(x_2, x_3) = (0.4, 1.2)$ plane the peak density is larger than in the $(x_2, x_3) = (0.4, 0.4)$ plane which lies closer to the boundary. This may be a reflection of the strongly reduced average action density near the boundary (cf. Sec. III D and Fig. 3). Statistical fluctuations are too large to substantiate this conjecture, however, as indicated by the fact that no such dilution is recognizable in Fig. 6 close to the boundaries in the x_1, x_4 directions.

Another instructive property of the dimeron field configurations is their amount of local selfduality. This feature

characterizes the interplay between the Yang-Mills dynamics and the topological charge density $q(x)$ (as defined in Eq. (23)) and can be monitored by evaluating the expression

$$R(x) = \frac{4}{\pi} \arctan \left(\sqrt{\frac{\text{tr} \{ F_{\mu\nu} F_{\mu\nu} - F_{\mu\nu} \tilde{F}_{\mu\nu} \}}{\text{tr} \{ F_{\mu\nu} F_{\mu\nu} + F_{\mu\nu} \tilde{F}_{\mu\nu} \}}} \right) - 1 \quad (18)$$

which varies from -1 at positions where the field is selfdual to $+1$ where it is anti-selfdual. Since for $g^2 = 1$ the strongly overlapping, regularized meron centers render the (anti-) dimerons almost (anti-) instanton-like, one expects that the peaks are approximately (anti-) selfdual while the surrounding regions, dominated by overlapping tails, are neither. The plots of $R(x)$ in the right panels of Fig. 6 confirm this expectation and thus allow to associate the action density peaks with either dimerons or anti-dimerons. Due to the one-to-one correspondence between the peaks in $s(x)$ and $R(x)$ the above comment on boundary effects applies here as well.

C. Topological charge distribution

We now proceed to a more quantitative analysis of the dimeron ensemble structure and its dependence on the square coupling g^2 . In the present section we look for patterns in the topological charge density which indicate short- and medium-range order. More specifically, we pick a pseudoparticle in a given ensemble configuration and measure the average density of the surrounding pseudoparticles with either equal or opposite topological charge, as a function of their distance from the selected one [75]. We then repeat this procedure for all pseudoparticles in the configuration and average over the obtained density profiles, again for equal and opposite topological charge separately. After finally averaging over all configurations of the $g^2 = 1$ ensemble we end up with the two distance profiles ρ_D plotted in the left panel of Fig. 7. The analogous procedure, but with the pseudoparticles replaced by individual meron centers, yields the profiles ρ_M shown in the right panel. The integral of these densities over the full ensemble is normalized to one. (The smallest and largest distances are excluded in both figures since they correspond to tiny shell volumes (inside the ensemble volume) in which the densities cannot be reliably estimated.) Figures 8 and 9 contain the same profiles as Fig. 7, but for $g^2 = 25$ and $g^2 = 100$.

The averaged radial density profiles reveal an intriguing amount of structure in the pseudoparticle distribution and in its meron substructure. First of all, the left panels of Figs. 7 – 9 show a depletion of both dimeron and anti-dimeron densities in the overlap region with the reference (anti-)dimeron. Hence they provide direct evidence for a strong short-distance repulsion between dimerons of any topological charge. This repulsion is sensitive to the relative color arrangement between neighboring pseudoparticles (cf. Sec. IV D) and may at least partly be caused by our limited field configuration space. A similar repulsive core (with a logarithmic distance dependence) shows up in superpositions of instantons and anti-instantons in singular gauge [46]. On a practical level, it helps to avoid clustering among the pseudoparticles and promotes smoother and more semiclassical ensemble configurations. Evidence for the latter was already encountered in the density plots of Sec. IV B.

At larger distances, a remarkable medium-range order emerges among the pseudoparticles for $g^2 = 1$ (left panel of Fig. 7). In fact, about one meron size $\rho \sim 0.55$ (or the slightly larger average dimeron size $\rho + \langle |a| \rangle$) from the fixed reference particle one finds an enhanced (depleted) density of pseudoparticles with opposite (equal) topological charge. At about 2ρ this structure is inverted and attenuated, i.e. the density of pseudoparticles with equal (opposite) charge is weakly enhanced (depleted). A further, even weaker inversion of the densities is discernible at distances $\sim 3\rho$, while from $d \gtrsim 3.5\rho$ both dimeron and antidimeron densities remain within errors equal to those of a random distribution. The almost periodic density oscillations over three consecutive layers indicate a pronounced mid-range order among the dimerons. In fact, the emerging shell structure resembles Debye-type screening clouds and indicates the existence of attractive short-distance correlations between dimerons and anti-dimerons [76].

The above screening behavior should be enhanced at $g^2 = 1$ where the entropy is lowest and the field configurations therefore most strongly ordered. This can indeed be seen in our results. While for $g^2 = 1$ the third shells are clearly visible in Fig. 7 (although less pronounced than the first two), they essentially disappear for $g^2 \geq 25$ (cf. Figs. 8 and 9). Moreover, the dimeron densities in the left panels of Figs. 8 and 9 show a weaker first shell at somewhat larger distances (reflecting the growing average size of the dimerons), which now slightly favors pseudoparticles of equal topological charge. A hint of a second shell with inverted topological charge remains recognizable as well. Hence at stronger coupling and over typical nearest-neighbor distances the (anti-) dimerons show a tendency to surround themselves with (anti-) dimerons. This behavior could be another indication for the with growing dimeron dissociation increasing role of the meron centers as the dynamically relevant degrees of freedom.

In order to test the latter interpretation, we show in the right panels of Figs. 7 – 9 the analogous density profiles ρ_M for individual meron centers (without regard for the dimerons which they are part of). At the smallest distances

$d \ll \rho$, i.e. in the immediate overlap region with the fixed reference meron, the nearest-neighbor meron is most likely its partner from the same dimeron, and hence has the same topological charge. This explains the enhanced (suppressed) density of equally (oppositely) charged merons for $d \ll \rho$. The enhancement is maximal for $g^2 = 1$ (cf. Fig. 7) where the mean inter-meron distance $2 \langle |a| \rangle$ is minimal, and decreases due the growing $\langle |a| \rangle$ with increasing g^2 . Outside of the immediate overlap region, on the other hand, i.e. for distances $d > \rho$, the meron density profiles in the right panels of Figs. 7 – 9 follow those of the corresponding dimeron densities (left panels) rather closely. This is expected because for $d > \rho$ the encountered merons belong more likely to different dimerons. Since for $g^2 = 1$ with $2 \langle |a| \rangle \simeq 0.27 \sim \rho/2$ the meron partners of the dimerons overlap almost completely, furthermore, their densities outside the immediate neighborhood of the reference meron should match those of the dimerons most closely, as is indeed the case.

We have already pointed out that the strongest intermediate-range order among the dimerons exists in the $g^2 = 1$ ensemble with its particularly low entropy. For a more systematic analysis of the changes in this behavior with increasing coupling we now proceed to the investigation of global ensemble properties. (Their smaller statistical error simplifies the study of the g^2 dependence.) We first consider the fraction $f_{\overline{D\overline{D}}}$ of dimerons in a given configuration whose nearest neighbor has opposite topological charge [77]. The ensemble-averaged probability $\langle f_{\overline{D\overline{D}}} \rangle$ is plotted in Fig. 10 for our five g^2 values between one and infinity. (The vertical line indicates a break in the scale of the abscissa which allows to include the strong-coupling limit $g^2 = \infty$.) For $g^2 = 1$ one reads off $\langle f_{\overline{D\overline{D}}} \rangle \simeq 87\%$. This large fraction confirms the strong preference of the dimerons to surround themselves with screening clouds consisting mostly of their anti-pseudoparticles. Already at $g^2 = 25$ the value of $\langle f_{\overline{D\overline{D}}} \rangle$ has diminished by half, however, to about 43%. This is a clear indication for the with increasing coupling growing disorder in the field configurations. It manifests itself not the least in the stronger dissociation of the dimerons ($2 \langle |a| \rangle \simeq 0.57 \simeq \rho$ at $g^2 = 25$, cf. Table II) which gradually replaces the interactions between dimeron centers by interactions between the increasingly independent meron centers. The fact that $\langle f_{\overline{D\overline{D}}} \rangle$ remains within errors around 45% for $g^2 = 100$ and 1000 signals the slight preference for equally charged pseudoparticle neighbors at stronger couplings, as already encountered in Figs. 8 and 9. At these couplings the dimerons are so far dissociated, however, that correlations between their centers do probably no longer characterize the main interactions which they experience. In any case, the non-interacting value of 50% for $\langle f_{\overline{D\overline{D}}} \rangle$ is attained only in the strong-coupling limit, i.e. in the random ensemble with $g^2 = \infty$ (notwithstanding additional boundary effects which come into play for maximally dissociated dimerons, cf. Sec. III D).

Further insight into the topological charge distribution of dimeron ensembles and its coupling dependence can be obtained from the average distances $\langle d \rangle$ between the pseudoparticle centers and their nearest neighbors with either equal or opposite topological charge. The nearest-dimeron distances are drawn in the left panel of Fig. 11 as a function of the square coupling g^2 . (They are evaluated in the same spherical shells as in Fig. 10.) For $g^2 = 1$ one finds the average distance $\langle d \rangle \simeq 0.71$ between oppositely charged neighbors to be about 25% smaller than that between equally charged ones ($\langle d \rangle \simeq 0.93$). This is a reflection of the screening clouds found above. After increasing the square coupling to $g^2 = 25$, on the other hand, the two distances have become almost identical. The nearest pseudoparticles of equal charge are now somewhat closer, as expected from the drop of $\langle f_{\overline{D\overline{D}}} \rangle$ below 50%. (The average distance to the next dimeron of any charge remains relatively constant, though.) This seems to be another consequence of the larger inter-meron separation $\langle 2 |a| \rangle \simeq 0.6 - 3.1$ for $g^2 = 25 - \infty$ and the increasing dynamical importance of the meron centers. (For close-to-maximally dissociated dimerons the mentioned boundary effects will distort the nearest-neighbor distances as well, cf. Sec. III D.)

Above we have found several pieces of evidence for the merons to gradually turn into the dynamically relevant degrees of freedom when the coupling increases. In order to explore this issue from yet another angle, we further computed the average distances between nearest-neighbor meron centers, as plotted in the right panel of Fig. 11. In the $g^2 = 1$ ensemble with its highly contracted pseudoparticles, nearest-neighbor merons belong most likely to the same dimeron and thus carry identical topological charge. As a consequence, the average separation between equally charged neighbor merons is almost the same as the distance $2 \langle |a| \rangle \simeq 0.27$ between partner merons. Oppositely charged neighbor merons, on the other hand, are more than twice as far separated, i.e. about as far as the average distance $\langle d \rangle \simeq 0.59$ between nearest-neighbor dimerons of opposite charge (cf. left panel of Fig. 11). Again, this picture changes significantly with increasing coupling. As the dimerons dissociate farther, the average distance $\langle d \rangle$ between equally charged nearest-neighbor merons must increase as well. However, it does so more slowly than the average separation $2 \langle |a| \rangle$ of the meron partners. This provides additional evidence for the interaction between individual merons belonging to different dimerons to increasingly determine the ensemble properties. At $g^2 = 25$ the average distance between oppositely charged nearest-neighbor merons has not yet decreased much, on the other hand. The main drop happens between $g^2 = 25$ and 100. From about $g^2 = 1000$ the distances $\langle d \rangle$ between equally and oppositely charged merons coincide and slightly increase together on the approach to the strongly-coupled random ensemble.

D. Color correlations

In the previous subsections we have found diverse spacial correlations in dimeron ensemble configurations and studied their coupling dependence. It remains to explore correlations between the color orientations of the dimerons to which we turn in the present section. There are several reasons for expecting these correlations to be significant. First, the “hedgehog”-type coupling between the spacetime and color dependence of the individual dimerons (cf. Eq. (5)) suggests that spacial and color correlations will be at least partly linked in the ensemble configurations as well. In fact, we have encountered a prototype of such correlations when studying the color-orientation dependence of the classical interaction energy between two isolated dimerons. In weakly coupled ensembles, furthermore, the almost completely contracted dimerons will experience interactions and correlations similar to those found in singular-gauge instanton ensembles (see below). In the strong-coupling regime, on the other hand, where the dimerons are dissociated and single merons with their long-range tails become dominant, one may expect color correlations of similar strength and importance as in the meron and regular-gauge instanton ensembles of Refs. [14, 19].

In order to characterize the $SU(2)$ color orientation between two neighboring dimerons with color coordinates c_β and c'_β (cf. Eq. (11)), we introduce the angle

$$\alpha := 2 \arcsin \left(\frac{1}{2} \sqrt{(c' - c)_\beta (c - c')_\beta} \right) \quad (19)$$

(with $\alpha \in [0, \pi]$) under which half of the geodesic distance between the two corresponding points on the group manifold S^3 (of unit radius) appears from the center. We then find for every pseudoparticle in a given ensemble configuration the nearest neighbors with equal and opposite topological charges, separately calculate the angles (19) between them and finally average over the configuration (excluding double-counting of pairs) and over the $g^2 = 1$ ensemble.

The resulting $\langle \alpha \rangle$ distributions are divided into 20 bins and plotted in Fig. 12 for both equally and oppositely charged neighbors. For comparison, we also show the angle distribution of the non-interacting $g^2 = \infty$ random ensemble. All three distributions are relatively broadly peaked at $\langle \alpha \rangle = \pi/2$. This happens even in the random ensemble, which indicates that this peak position is statistically favored. Indeed, $\alpha = \pi/2$ corresponds to the equator of S^3 and thus to the α value with the maximal number of color orientations. The main lesson of Fig. 12 is, however, that equally and oppositely charged dimeron neighbors on average prefer remarkably different relative color orientations. While the distribution of the mean color angle $\langle \alpha_{D\bar{D}} \rangle$ between nearest neighbors of opposite Q is essentially consistent with a random distribution, the peak value of the $\langle \alpha_{DD, \bar{D}\bar{D}} \rangle$ distribution for neighbors of equal Q is dynamically enhanced by about a factor of two.

These results can be rather directly understood by recalling that the interactions between the strongly contracted dimerons in the rather dilute $g^2 = 1$ ensemble (with $\langle d \rangle > \rho$, cf. Fig. 11) are similar to those among instantons in singular-gauge instanton-antiinstanton superpositions [23, 46]. Between instantons of equal topological charge these classical interactions $\Delta S_{II, \bar{I}\bar{I}}$ are repulsive for any relative color orientation. More specifically, at distances $d > \rho$ one has [46]

$$\Delta S_{DD, \bar{D}\bar{D}} \stackrel{g^2=1}{\sim} \Delta S_{II, \bar{I}\bar{I}} = \frac{32\pi^2}{g^2} \left[2 + \left(1 - 2 \sin^2 \frac{\alpha}{2} \right)^2 \right] \frac{\rho^6}{d^6} + O \left(\frac{\rho^8}{d^8} \right). \quad (20)$$

Since the average distance between DD and $\bar{D}\bar{D}$ pairs in our $g^2 = 1$ ensemble is $\langle d_{DD, \bar{D}\bar{D}} \rangle \simeq 0.93 \sim 2\rho$ (cf. Fig. 11), the leading term in Eq. (20) should reasonably well approximate $\Delta S_{DD, \bar{D}\bar{D}}$. The resulting α distribution is thus symmetric around $\pi/2$ and the individual repulsion is minimal (maximal) at $\alpha = \pi/2$ ($\alpha = 0, \pi$). Hence the average repulsion in the ensemble is reduced by more strongly populating the $\alpha \simeq \pi/2$ color orientations. This explains the enhanced peak around $\langle \alpha_{DD, \bar{D}\bar{D}} \rangle = \pi/2$ in Fig. 12.

The instanton-anti-instanton interactions in singular-gauge instanton superpositions, on the other hand, contain the for $d > \rho$ leading dipole-dipole interaction [46]

$$\Delta S_{D\bar{D}} \stackrel{g^2=1}{\sim} \Delta S_{I\bar{I}} = -\frac{32\pi^2}{g^2} \left[1 - 4 \left(c_\mu \hat{d}_\mu \right)^2 \right] \frac{\rho^4}{d^4} + O \left(\frac{\rho^6}{d^6} \right) \quad (21)$$

where the unit vector \hat{d}_μ points from the instanton center to the anti-instanton center. For spacial and color orientations with $|c_\mu \hat{d}_\mu| < 1/2$, which are predominant in the $g^2 = 1$ equilibrium ensemble, the leading term in Eq. (21) is attractive. In fact, indirect evidence for this attraction was already deduced from our dimeron distributions in Sec. IV C. All remaining $I\bar{I}$ interactions are repulsive, on the other hand, as those between equally charged neighbors. In contrast to the latter case, however, the impact of $\Delta S_{D\bar{D}}$ on the $\langle \alpha_{D\bar{D}} \rangle$ distribution is less transparent since the strength of the $D\bar{D}$ attraction is not determined by α . Moreover, the relatively small average dimeron-antidimeron

distance $\langle d_{D\bar{D}} \rangle \simeq 0.7 \sim 3\rho/2$ for $g^2 = 1$ (cf. Fig. 11) indicates that the repulsive terms of $O(\rho^6/d^6)$ remain relevant as well. Therefore it seems likely that this repulsion, together with the overall short-distance repulsion (cf. Sec. IV C) and the ensemble entropy, on average compensates at least part of the leading attraction. The resulting *averaged* DD correlations should thus be considerably weaker than those in the DD and $D\bar{D}$ channels. As a consequence, the $\langle \alpha_{D\bar{D}} \rangle$ distribution will be close to that of a random ensemble, and this is indeed what we observe in Fig. 12.

The above reasoning focused on two-pseudoparticle forces. This is legitimate because many-body interactions in the rather dilute $g^2 = 1$ ensemble are suppressed by the small packing fraction of the contracted dimers and by their reduced overlap. Moreover, the emerging parallels with the color correlations in instanton-anti-instanton superpositions reinforce our premise that the properties of weakly coupled dimeron ensembles indeed approach those of instanton liquid models. As already alluded to, the above arguments further suggest that the smaller average distance $\langle d_{D\bar{D}} \rangle < \langle d_{DD, \bar{D}\bar{D}} \rangle$ between oppositely charged dimers and the related screening-cloud arrangement in the $g^2 = 1$ ensemble (cf. Sec. IV C) are mainly caused by attractive color-dipole interactions. With growing coupling and entropy, however, the relative impact of the potentials (20) and (21) on the free energy and on the ensemble structure decreases. This holds in particular for the DD attraction which has the longest range. Our finding of $\langle d_{D\bar{D}} \rangle \sim \langle d_{DD, \bar{D}\bar{D}} \rangle$ for $g^2 \gtrsim 25$ (cf. Fig. 11) indeed indicates that the common repulsion in both DD and $DD, \bar{D}\bar{D}$ channels and the growing entropy begin to dominate at larger couplings. One would thus expect the peak in the $\langle \alpha_{DD, \bar{D}\bar{D}} \rangle$ distribution to broaden with increasing coupling until the random distribution is reached for $g^2 \rightarrow \infty$. The $\langle \alpha_{D\bar{D}} \rangle$ distribution, on the other hand, may become somewhat more sharply peaked at larger g^2 when the compensating impact of the attraction subsides.

In order to test these expectations and to shed further light on the coupling dependence of the color correlations, we have evaluated the standard deviation $\sqrt{\Delta \langle \alpha \rangle}$ of the $\langle \alpha \rangle$ distribution from its (g independent) mean value $\langle \alpha \rangle = \pi/2$. In Fig. 13 we plot $\sqrt{\Delta \langle \alpha \rangle}$, again separately for equally and oppositely charged neighbor dimers, at five g^2 values. For $g^2 = 1$ the standard deviation of the $\langle \alpha_{DD, \bar{D}\bar{D}} \rangle$ distribution reaches only about half of that of the $\langle \alpha_{D\bar{D}} \rangle$ distribution, in agreement with its higher and narrower peak in Fig. 12. Also expected from Fig. 12 is that the $g^2 = 1$ value of $\sqrt{\Delta \langle \alpha_{D\bar{D}} \rangle}$ remains close to the random ensemble value at $g^2 = \infty$. In fact, the width of the $\langle \alpha_{D\bar{D}} \rangle$ distribution decreases only little with growing coupling, as anticipated above, until $\langle \alpha_{D\bar{D}} \rangle$ becomes randomly distributed. The width of the $\langle \alpha_{DD, \bar{D}\bar{D}} \rangle$ distribution, on the other hand, grows rather strongly with g^2 on its approach to the random value, again confirming our above expectations. Nevertheless, even at $g^2 = 1000$ the $\langle \alpha_{DD, \bar{D}\bar{D}} \rangle$ distribution remains significantly more peaked than the random distribution. Hence some of the stronger average repulsion between nearest-neighbor dimers of equal topological charge seems to remain influential even at these rather large couplings (see also Sec. IV C).

Reflecting upon the above analysis one may wonder to what extent pertinent features of the α distributions are obscured by taking the configuration and ensemble averages. Indeed, the spacial averaging and the interplay between spacial and color correlations may wash out interesting local features of the relative color ordering. However, one would expect this type of leveling to be weakest in the $g^2 = 1$ ensemble where the almost spherical color distribution of the dimers is most concentrated and the impact of their spacetime orientation consequently minimized. Other qualitative effects of the stronger intermediate-range order among neighboring dimers at $g^2 = 1$ may therefore also be robust enough to survive the averaging procedure.

E. Topological susceptibility

The topological susceptibility χ_t characterizes several fundamental properties of the Yang-Mills vacuum. It governs, for instance, the dependence of the free energy on the CP violating vacuum angle θ around $\theta = 0$ and the mass of the η' meson in quantum chromodynamics with a large number N_c of colors [51]. Moreover, it contains information on the interplay between the Yang-Mills dynamics and the topology of the gauge group which was conjectured long ago to be the origin of linear quark confinement [21].

In a finite spacetime volume V , the topological susceptibility is defined as

$$\chi(V) = \frac{\langle Q(V) Q(V) \rangle}{V} \quad (22)$$

(which may contain contact terms [52] in the $\rho \rightarrow 0$ and $a \rightarrow 0$ limits) where $Q(V)$ is the topological charge of the gauge field in V , i.e.

$$Q(V) = \int_V d^4x q(x) \quad \text{with } q(x) = \frac{1}{16\pi^2} \text{tr} \{ F_{\mu\nu} \tilde{F}_{\mu\nu} \} \quad (23)$$

($\tilde{F}_{\mu\nu} \equiv \varepsilon_{\mu\nu\alpha\beta} F_{\alpha\beta}/2$). In the context of our vacuum description by topologically active constituents, χ is of particular interest because it quantifies the strength of topological charge fluctuations around $\langle Q \rangle = 0$. The latter is enforced

by CP symmetry which is sufficiently manifest in our ensembles because the configurations (13) contain a very nearly equal number of dimers and anti-dimers [78].

The topological susceptibility $\chi_t \equiv \lim_{V \rightarrow \infty} \chi(V)$ of SU(2) Yang-Mills theory is known from several independent high-precision lattice simulations [53, 54] (with their scale set by prescribing the value of the physical string tension). At large N_c , furthermore, the value of χ_t can be obtained either from lattice extrapolations [54–56] or from experimentally measured properties of the lightest pseudoscalar meson nonet. Indeed, to leading order in $1/N_c$ the Witten–Veneziano mechanism predicts [51]

$$\chi_{t, \text{SU}(N_c \rightarrow \infty)} \simeq \frac{f_\pi^2}{2N_f} (m_{\eta'}^2 + m_\eta^2 - 2m_K^2) \simeq (180 \text{ MeV})^4 \quad (24)$$

(where f_π is the pion decay constant, N_f is the number of flavors and $m_\eta, m_{\eta'}, m_K$ are the η, η' and K meson masses) and thereby relates $\chi_{t, \text{SU}(\infty)}$ to the part of the η' mass which does not originate from the strange-quark mass. The above values of χ_t will serve as benchmarks for comparison with our results and for scale-setting purposes.

To evaluate χ in our dimeron ensembles, we first compute the topological charge $Q(V)$ of each gauge-field configuration. More specifically, we integrate the topological charge density, obtained analytically from Eqs. (13) and (23), on a special grid [79] whose extent is varied in small steps to tune through the desired range of volumina V . The correlation between discretization errors in the two Q factors of χ (which arise from neglecting fluctuations with wavelengths below the grid-point distance in the coarse-grained density q) is reduced by evaluating the second factor on a modified grid. The latter is obtained by replacing each of the original grid-point positions with a randomly chosen one inside a surrounding volume determined by the inverse grid-point density. Finally, the ensemble average is carried out according to Eq. (22).

Translational invariance implies that $\chi(V)$ becomes volume-independent in the thermodynamic limit and that $\chi_t \equiv \lim_{V \rightarrow \infty} \chi(V)$ exists (after appropriate renormalization). In fact, this V independence will develop already in finite volumes whose linear dimensions $\sim V^{1/4}$ sufficiently much exceed the correlation length of the topological charge density. In order to test how far this applies to our simulation volumes and permits extrapolations of our $\chi(V)$ to $V \rightarrow \infty$, we have calculated $\chi(V)$ in a range of volumes in which boundary effects remain controllable. (Numerical efficiency is improved by varying only the temporal extent of the evaluation volumes. All three spacial dimensions of the boxes are kept fixed at 1.2 (chosen to limit boundary artefacts, cf. Sec. III D) and remain centrally embedded.)

The resulting volume dependence of the topological susceptibility is shown in Fig. 14 for $g^2 = 1$ and 100. In small volumes topological charge fluctuations are suppressed and $\chi(V)$ accordingly starts out close to zero. Towards our largest reliably accessible volumes, on the other hand, boundary effects may become relevant and begin to reduce χ . (Hence Fig. 14 contains independent information on the extent to which the boundary breaks translational invariance.) Nevertheless, for both coupling values $\chi(V)$ shows a rather broad maximum towards the end of the trustworthy V range. It is tempting to interpret these maxima as the onset of the expected saturation plateaus, and the corresponding χ values as reliable approximations to the infinite-volume predictions χ_t . However, from our data sets one cannot decide with confidence whether the maxima do not instead underestimate χ_t by interpolating between the rise of $\chi(V)$ at small V and its boundary-induced decline at large V . We shall therefore interpret the maximal values $\hat{\chi}$ (in this and the following sections a hat will indicate a dimensionful quantity given in our numerical units) more conservatively as lower bounds on the topological susceptibility.

| g^2 | $\hat{\chi}^{1/4}$ | a_χ [fm] | σ [fm ⁻²] |
|----------|--------------------|--------------------|------------------------------|
| 1 | 0.75 ± 0.032 | 0.076 ± 0.0032 | 3.864 ± 0.0793 |
| 25 | 0.83 ± 0.043 | 0.084 ± 0.0045 | 9.832 ± 0.7271 |
| 100 | 0.94 ± 0.032 | 0.095 ± 0.0033 | 9.340 ± 0.4518 |
| 1000 | 2.42 ± 0.083 | 0.246 ± 0.0096 | 3.363 ± 0.1051 |
| ∞ | 10.35 ± 0.503 | 1.043 ± 0.0508 | 0.1607 ± 0.0008514 |

TABLE III: (Lower bounds on) the fourth root of the topological susceptibility $\hat{\chi}$ in numerical units for five values of the squared gauge coupling. The last columns contain the grid constant a_χ and the string tension σ in physical units as obtained when setting the scale with the SU(2) Yang-Mills value $\chi^{1/4} = 0.99 \text{ fm}^{-1}$.

In Table III the corresponding values of $\hat{\chi}^{1/4}$ are listed with statistical (jackknife) error estimates for our five standard g^2 values. On a cautionary note, we recall that the $g^2 = 1$ dimeron ensemble thermalizes very slowly and that the autocorrelation for the topological charge becomes correspondingly large. The error of $\hat{\chi}^{1/4}$ as quoted in Table III does not take this strong autocorrelation into account and is therefore probably underestimated at least for $g^2 = 1$. With this caveat in mind, we observe that $\hat{\chi}^{1/4}$ stays inside our error estimates for $25 \leq g^2 \leq 100$ practically

constant (which becomes even more obvious when expressing $\chi^{1/4}$ in physical units, cf. Table V). This weak coupling dependence may be related to the similarly weak temperature dependence of the topological susceptibility in the confined phase of Yang-Mills theory up to the phase transition [56]. For larger g^2 our $\hat{\chi}^{1/4}$ values grow too strongly, on the other hand, which is at least in part due to boundary artefacts. Indeed, from $g^2 \gtrsim 1000$ the dimers are on average as far dissociated as the boundary allows. As discussed in Sec. III D, they then tend to accumulate along the box diagonals, with their centers concentrating in the middle of the box. These distorted field configurations break translational invariance almost everywhere in the simulation volume.

Our numerical results for the topological susceptibility provide a first opportunity to set the distance scale a in our box as a function of g^2 . To this end we write $a_\chi = \hat{a} (\hat{\chi}/\chi)^{1/4}$ in physical units, where $\hat{a} = 0.1$ and $\hat{\chi}$ are given in our numerical units while $\chi = (0.99)^4 \text{ fm}^{-4}$ is the SU(2) Yang-Mills value obtained from the SU(2) lattice result $\chi^{1/4}/\sigma^{1/2} = 0.483 \pm 0.006$ [54] in combination with the physical string tension $\sigma \simeq 4.2 \text{ fm}^{-2}$ [1]. The resulting values of a_χ in fm are listed in Table III. With their help one may convert our data e.g. for the string tension $\hat{\sigma}$ (cf. Table IV) via $\sigma = (\hat{a}/a_\chi)^2 \hat{\sigma}$ into physical units, as done in the last column of Table III.

A quantitative comparison of our results with those of other approaches in physical units will be postponed to Sec. IV G. For a first orientation, however, one may compare our “raw data” for $\hat{\chi}$ with their counterparts from the regular-gauge instanton and meron ensembles of Ref. [14] (which adopted $g^2 = 32$ and a size regulator $\rho \leq 0.1$) even though the physical distance scales might not be straightforwardly related. (In the ensembles of Ref. [14] about 90% of the topological susceptibility is generated by the peaks in the topological charge density associated with individual merons or regular-gauge instantons, incidentally; the remaining, smoother background field contributes just the remaining 10%.) According to Table III, our ensembles with $g^2 = 25 - 100$ give $\hat{\chi}^{1/4} \sim 0.8 - 0.9$ which is of the same order as the meron-ensemble result $\hat{\chi}^{1/4} = 0.77$ [14] for a comparable meron density in physical units, corresponding to $N_{M+\bar{M}} = 100$ (see below). In fact, at the above couplings $g^2 = 25$ and 100 our dimeron density reaches about half of Ref. [14]’s meron density and therefore yields a similar density of meron constituents. (The regular-gauge instanton ensemble with an instanton density roughly equal to our dimeron density (corresponding to $N_{I+\bar{I}} = 100$), on the other hand, generates the significantly larger value $\hat{\chi}^{1/4} \simeq 1.37$ [14].) Within errors the topological susceptibilities of meron and dimeron ensembles in numerical units are therefore consistent. As a consequence, setting scales by imposing a common “physical” value for χ will lead to comparable physical distance scales.

F. Wilson loops, static-quark potentials and string tension

The search for the conjectured transition of dimeron ensembles into confining meron ensembles is one of the central objectives of our study (cf. Sec. I). Our first quantitative evidence for the actual development of a meron-dominated phase was discussed in Sec. IV B where we found the dimers to dissociate into their progressively independent meron constituents when the coupling increases. We are now proceeding to the crucial question whether the gradually liberated merons indeed generate an area law for large Wilson loops and thus linear confinement with a finite string tension. More specifically, we are going to evaluate ensemble averages (i.e. vacuum expectation values) of path-ordered Wilson loops

$$W[C(R, T)] = \text{tr} \left(\mathcal{P} \exp i \oint_C A_\mu dx_\mu \right) \quad (25)$$

along closed, rectangular paths C . The latter correspond to the worldlines of fundamentally colored, static quark and antiquark sources, separated by a spacial distance R and evolving over the Euclidean time $T > R$. The static energy required to introduce and separate these sources in the vacuum is then given by the potential

$$V(R) = - \lim_{T \rightarrow \infty} \frac{1}{T} \ln \langle W[C(R, T)] \rangle. \quad (26)$$

Hence a linear rise of $V(R)$ for sufficiently large R signals linear quark confinement by color-flux tube formation.

Since we are particularly interested in the behavior of $V(R)$ at the largest reliably calculable R values, our strategy for computing W is designed to minimize the impact of boundary effects (as identified in Sec. III D) while still making efficient use of the ensemble configurations. This is achieved by restricting the evaluation volume to several subvolumina centered in the core box of Sec. III A. Artefacts of the boundary are reduced by limiting the extent of these volumina to 2.0 in the time direction, to 1.0 in the spacial R direction and to 0.5 in the two remaining spacial directions. The volumina generated by permutations of the spacial directions are included as well. As a consequence, fields in regions in which we diagnosed the main violations of translational invariance are excluded from the evaluation.

Next, we compute the oriented links $U[l(x \rightarrow x')] = \text{tr} \mathcal{P} \exp i \int_{l(x \rightarrow x')} A_\rho dx_\rho$ which connect neighboring grid points x_μ and x'_ν in the evaluation volume by straight lines $l(x \rightarrow x')$. All rectangular Wilson loops with aspect ratio $R/T = 1/2$ are then constructed from combinations of these color parallel transporters. (For small enough loops we exploit Euclidean symmetry to assign the time direction to the longer side, irrespectively of its orientation in the core box.) In order to obtain quantitative information about the impact of boundary and resolution errors on the reliability of the link calculation, we perform the latter both (i) on the full subvolumina described above, with the R values progressing in steps of length 0.1, and (ii) just on the central hyperplanes of these volumina, spanned by the longer spacial direction (with length 1.0) and the temporal direction, in which the R values progress with step size 0.025.

The main challenge for our finite grid resolution arises from gauge fields along a link which develop unusually large gradients by approaching a meron center, as already alluded to in Sec. III D. Since this turns out to happen relatively rarely, we decided to dynamically adapt the resolution of the grid on which the gauge fields are sampled along the link. The refined grid then increases the accuracy of the numerical integration in the link exponent. We start with a maximal grid-point distance of 0.01, i.e. on a grid which is 10 times finer than the one on which the gauge-field configurations were generated. This distance is reduced by half if the Frobenius norm of the difference between a given link and the path-ordered product of two links over half the distance exceeds one per mille, i.e. if

$$\|U[l(x_\mu \rightarrow x_{\mu+1})] - U[l(x_\mu \rightarrow x_{\mu+1/2})] U[l(x_{\mu+1/2} \rightarrow x_{\mu+1})]\| \geq 0.001. \quad (27)$$

The criterion (27) is chosen such that about one third of the links in an average Wilson loop has to be updated at least once. (Two refinement updates of the subgrid for the same link are almost never encountered with our regulator $\rho^2 = 0.3$.) Finally, we calculate the average over all Wilson loops [80] with the same edge length R and evaluate the logarithm $\ln \langle W[C(R, 2R)] \rangle$ of their ensemble average.

In Fig. 15 the resulting data are plotted as a function of the loop area $A = 2R^2$ for our five square couplings $g^2 = 1, 25, 100, 1000$ and ∞ . The figure includes the points obtained from both the full subvolumina and their central hyperplanes, which agree within errors [81]. It further shows the best fits of the $\ln \langle W \rangle$ data to the function

$$f(A) = \hat{\omega} + \hat{\tau}P(A) - \hat{\sigma}A \quad (28)$$

where $P(A) = 3\sqrt{2A}$ is the perimeter of the rectangular loops. The ansatz (28) may e.g. be motivated by a string model which takes small, UV-regularized quantum fluctuations into account [14, 57]. All fit results are collected in Table IV, together with their χ^2 values per degree of freedom and the fit ranges $A \in [A_{\min}, A_{\max}]$ in which the data are probably reliable. The χ^2 values indicate that the fits indeed allow for a reliable determination of the parameters $\hat{\omega}$, $\hat{\tau}$ and in particular of the string tension $\hat{\sigma}$. The central lesson of these results is that dimeron ensembles indeed generate finite string tensions which monotonically increase with g^2 . Our findings in Secs. IV A – IV D explain this increase as a consequence of the dimerons' gradual release of their disordering meron tails. In addition, our results provide evidence for dimeron dissociation to trigger the transition from a non-confining regime to a confining phase. (In the thermodynamic limit the analogy with Kosterlitz-Thouless-type transitions suggests that the string tension will vanish exactly below some critical value g_c^2 . In finite volumes one expects a more gradual transition, however, as seen in our data.)

| g^2 | $\hat{\omega}$ | $\hat{\tau}$ | $\hat{\sigma}$ | χ^2 | A_{\min} | A_{\max} |
|----------|------------------|-----------------|------------------|----------|------------|------------|
| 1 | -0.22 ± 0.09 | 0.27 ± 0.07 | 2.23 ± 0.22 | 0.22 | 0.20 | 1.60 |
| 25 | -0.51 ± 0.04 | 0.81 ± 0.04 | 6.95 ± 0.21 | 0.32 | 0.10 | 0.90 |
| 100 | -0.20 ± 0.01 | 0.55 ± 0.02 | 8.47 ± 0.18 | 0.44 | 0.03 | 0.51 |
| 1000 | -0.02 ± 0.04 | 0.47 ± 0.08 | 20.08 ± 0.66 | 0.21 | 0.03 | 0.35 |
| ∞ | -0.63 ± 0.09 | 0.23 ± 0.20 | 17.57 ± 1.80 | 1.06 | 0.01 | 0.35 |

TABLE IV: Results for the parameters $\hat{\omega}$, $\hat{\tau}$ and the string tension $\hat{\sigma}$, obtained from the fit of $f(A)$ to $\ln \langle W \rangle(A)$ in the interval from A_{\min} to A_{\max} . (The reduced chi-square value χ^2 characterizes the statistical goodness of the fit and should not be confused with the square of the topological susceptibility.)

We have additionally applied a somewhat complementary method of computing the string tension. In this approach the static quark-antiquark potential $V(R)$ is extracted directly from the Wilson-loop behavior according to Eq. (26). This allows us to include loops of multiple aspect ratios, provides a useful cross check on our results for $\hat{\sigma}$ in Table IV and makes it possible to obtain physical information from the small- R behavior of V as well. To implement this approach we evaluate rectangular loops of all aspect ratios which fit into the subvolumina defined above. The value of V at a given R is then extracted from a fit of $\ln \langle W \rangle / T$ to a constant inside the $T \gtrsim R$ ranges in which $\ln \langle W \rangle / T$

becomes approximately T independent. The resulting potentials are plotted in Fig. 16 for $g^2 = 1, 25$ and 100 . All $V(R)$ curves indeed show an essentially linear rise for $R \gtrsim 0.4$. (Due to growing boundary effects, the potentials cannot be reliably extracted beyond a coupling-dependent $R_{\max} \gtrsim 0.7 - 1$.) It is reassuring, furthermore, that fits to the linear region yield values for the string tension ($\hat{\sigma}(g^2 = 1) \simeq 1.6$, $\hat{\sigma}(g^2 = 25) \simeq 6.3$ and $\sigma(g^2 = 100) \simeq 9.3$) which are within 10 – 20% of those with better statistics given in Table IV.

Before setting scales and comparing to results of other approaches in Sec. IV G, we may get a first idea of the quantitative significance of our $\hat{\omega}, \hat{\tau}$ and especially $\hat{\sigma}$ values by comparing them to their counterparts in the meron and regular-gauge instanton ensembles of Ref. [14] (which adopted $g^2 = 32$, $\rho \leq 0.1$ and $N_{I+\bar{I}, M+\bar{M}} = 500$). The meron ensemble yields $\hat{\omega} = -0.5$, $\hat{\tau} = 0.94$ and $\hat{\sigma} = 12.8$ which are overall closest to our $g^2 = 25$ and 100 results. However, the string tension in the meron ensemble exceeds ours in the $g^2 = 100$ dimeron ensemble by about 50%. This is probably because our dimerons' constituent merons are not yet fully liberated at $g^2 = 25 - 100$ (cf. Table II) and because their density is somewhat lower than the meron density in the $N_{M+\bar{M}} = 500$ ensemble of Ref. [14]. In any case, the “raw” data suggest that the confinement properties of $g^2 = 32$ meron and $g^2 = 25 - 100$ dimeron ensembles are at least qualitatively compatible. (Another indication may be that the string tensions in both meron and dimeron ensembles roughly double in the strongly-coupling limit, boundary effects notwithstanding. The results $\omega = -0.1$, $\tau = 0.58$, $\sigma = 20.5$ for the regular-gauge instanton ensemble [14], incidentally, turn out to reproduce ours from the $g^2 = 1000$ dimeron ensemble up to a few percent.)

The above considerations indicate that fixing the string tension at a common physical value will result in comparable confinement scales of both meron and dimeron ensembles in the $g^2 = 25 - 100$ coupling region. This is reassuring because the linear rise of our $V(R)$ should then rather directly match on to the linear potential of the meron ensemble even at $R \gtrsim 1$, where the confining flux tube is expected to develop fully but where we cannot reliably extract it from our present data set. This expectation is supported by fits of the meron-ensemble result for $V(R)$ to a regularized string model in an extended R range including $R > 1$ [14]. In fact, within errors those fits reproduce the string tension obtained from fitting $\ln \langle W \rangle$ to Eq. (28) in an A range with a smaller $R_{\max} = \sqrt{A/2}$ than ours. This indicates that our string tension can indeed be reliably determined by fitting Eq. (28) in a region of relatively small areas. It also adds considerably to the evidence for dimeron ensembles to provide a viable pathway towards confining meron ensembles.

We close this section with a few comments on the small- R behavior of $V(R)$ which is of physical interest in its own right. For $R \lesssim 0.4$ our potentials exhibit to a good approximation a quadratic R dependence which extends farthest for $g^2 = 1$ and is little affected by boundary artefacts. In order to understand this behavior one should recall that such a quadratic small- R potential [82] is generated by sufficiently dilute instanton-antiinstanton ensembles [24–26]. This indicates that for $R \lesssim \rho$ our $V(R)$ are dominated by contributions from little dissociated dimerons which behave essentially as singular-gauge instantons. (Table II and the dimeron density estimates in Sec. IV G suggest that our ensembles keep a substantial fraction of such instanton-like dimerons even at larger couplings.) For a more quantitative consistency check we recall that a dilute SU(2) instanton ensemble generates the short-distance behavior $V(R) \simeq 0.5\rho^{-3}R^2$ [24], i.e. $V(R) \simeq 2.8 R^2$ for our size parameter $\rho = 0.55$. From a quadratic fit to our $g^2 = 1$ potential at distances $R \lesssim 0.4$, on the other hand, we obtain $V(R) \simeq 3.8 R^2$ which is indeed of the same order.

G. Dimensionless amplitude ratios and results in physical units

A quantitative comparison of the dimensionful amplitudes and observables calculated above with those of other approaches requires either to form dimensionless combinations of our results or to rewrite them in physical units. Both will be done in the present section. We start with the discussion of three dimensionless ratios which can be formed from our results and thus compared to other data without scale-setting ambiguities.

Our first example is the ratio $\langle \hat{s} \rangle / \hat{\sigma}^2 = \langle s \rangle / \sigma^2$ of the ensemble-averaged Yang-Mills action density $\langle \hat{s} \rangle$ (the hat again indicates numerical units) and the appropriate power of the string tension given in Table IV. The density $g^2 \langle \hat{s} \rangle$ is (modulo renormalization issues) proportional to the gluon condensate $\langle F^2 \rangle$ and therefore of considerable interest in its own right. Our results for $g^2 \langle \hat{s} \rangle$ can be obtained from the values computed in Sec. III D on diagonals through the simulation volume by taking the average values of the plateau fits in Figs. 3 and 4, i.e. $g^2 \langle s \rangle (g^2 = 1) \simeq 210$ and $g^2 \langle s \rangle (g^2 = 25) \simeq 425$. With the results for $\hat{\sigma}$ in Table IV this yields $\langle s \rangle / \sigma^2 (g^2 = 1) \simeq 94$ and $\langle s \rangle / \sigma^2 (g^2 = 25) \simeq 3$. The latter value corresponds to the coupling range $g^2 \simeq 25 - 100$ in which the dimeron ensembles were estimated above to best approximate the confining phase of the Yang-Mills vacuum. Hence this value should be compared to the SU(2) lattice value $\langle s \rangle / \sigma^2 \simeq 4.5$ [60], the QCD sum-rule values $\langle s \rangle / \sigma^2 \simeq 4 - 10$ [49] (which correspond to $N_c = 3$ and contain quark corrections, however) and the value $\langle s \rangle / \sigma^2 \simeq 8$ [83] in the meron ensemble [14]. (The regular-gauge instanton ensemble yields $\langle s \rangle / \sigma^2 \simeq 10$ [14].). Of course, all these values should be taken with a grain of salt since they involve large subtractions whose systematic error cannot be reliably estimated. In any case, within expected

errors our result for $g^2 = 25$ is compatible with the SU(2) lattice value and several QCD sum-rule estimates.

A second useful dimensionless ratio to be assembled from our results is $\chi / (g^2 \langle s \rangle)$. In fact, there has been a proposal for an approximate low-energy relation in Yang-Mills theory, $\chi \simeq \langle F^2 \rangle / (66\pi^2 N_c)$ [61], which would fix this ratio as $\chi / (g^2 \langle s \rangle) \simeq 1 / (33\pi^2) \simeq 3.07 \times 10^{-3}$ (for $N_c = 2$ and with $g^2 \langle s \rangle = \langle F^2 \rangle / 4$). A dilute-instanton-gas estimate similarly yields $\chi / (g^2 \langle s \rangle) \simeq 1 / (32\pi^2)$ [84]. With the SU(2) Yang-Mills lattice result $\chi^{1/4} / \sigma^{1/2} = 0.483 \pm 0.006$ [54] and the ratio quoted above one arrives at the similar value $\chi / (g^2 \langle s \rangle) \simeq 3.21 \times 10^{-3}$ while the range of condensate results $\langle F^2 \rangle \simeq 0.1 - 0.3 \text{ GeV}^4$ [49] from QCD sum-rule analyses (corresponding to $N_c = 3$ and containing quark admixtures) together with the SU(2) Yang-Mills value $\chi^{1/4} \simeq 195 \text{ MeV}$ (see below) yields $\chi / (g^2 \langle s \rangle) \simeq (1.2 - 3.6) \times 10^{-3}$. From the data for $\hat{\chi}$ in Table III and for $\langle \hat{s} \rangle$ as given above, finally, our dimeron ensemble results are $\chi / (g^2 \langle s \rangle) \simeq 1.9 \times 10^{-3}$ for $g^2 = 1$ and $\chi / (g^2 \langle s \rangle) \simeq 1.2 \times 10^{-3}$ for $g^2 = 25$, within the range obtained from the sum-rule values for the gluon condensate but smaller than the lattice value.

The third dimensionless quantity which can be formed from our results is $\chi^{1/4} / \sigma^{1/2}$. In contrast to the ratios discussed above, it has the additional benefit of not involving the rather unreliably known and renormalization-scale dependent expectation value of the action density. Our $\chi^{1/4} / \sigma^{1/2}$ values for the five different g^2 are listed in Table V. The inverse ratio $\sigma^{1/2} / \chi^{1/4}$ is plotted for the four finite g^2 values in Fig. 17. For g^2 between 1 and 1000 our values for $\chi^{1/4} / \sigma^{1/2}$ lie in the range from 0.3 to 0.55. Hence they are indeed rather compatible with the SU(2) lattice value $\chi^{1/4} / \sigma^{1/2} = 0.483 \pm 0.006$ [54]. Moreover, for $g^2 = 25 - 100$ our results are practically identical to the meron-ensemble value $\chi^{1/4} / \sigma^{1/2} \simeq 0.31$ [14] at $g^2 = 32$ (and somewhat smaller than the range $0.42 \leq \chi^{1/4} / \sigma^{1/2} \leq 0.48$ obtained from regular-gauge instanton ensembles [14]).

Since correlations among individual observables may be hidden in the dimensionless ratios discussed above, it is also important to directly compare dimensionful results in physical units with those of other approaches. For this purpose, we have considered two alternative scale-setting procedures. The first was introduced in Sec. IV E and prescribes a standard value for the topological susceptibility in SU(2) Yang-Mills theory. This allows to rewrite our results for the string tension in physical units, as given in the last column of Table III. For $g^2 = 25 - 100$ they are roughly twice as large as those obtained from Regge phenomenology (see below), while for $g^2 = 1000$ our value is about 25% smaller. Continuing this trend, the string tension becomes unnaturally small in the strong-coupling limit, as a consequence of $\hat{\chi}$ growing too large due to boundary artefacts (cf. Sec. IV E and below).

In the following, we therefore adopt a more standard approach to scale setting which fixes the string tension at its physical value $\sigma \simeq 4.2 \text{ fm}^{-2}$ (estimated from the almost universal experimental Regge slopes [1]). This amounts to writing our discretization scale in physical units as $a = \hat{a} (\hat{\sigma} / \sigma)^{1/2}$, with $\hat{a} = 0.1$ and $\hat{\sigma}$ (cf. Table IV) given in numerical units. The resulting values in Table V show that a increases with g^2 . Hence the resolution of short-distance features in the vacuum field population decreases moderately with the coupling. This tendency is enhanced by the gradual dissociation of the well-localized, singular-gauge dimerons into broader merons (cf. Sec. IV A) which contain less short-wavelength Fourier modes. As argued above, we expect our ensembles to best reproduce observables in the confining Yang-Mills vacuum phase for $g^2 = 25 - 100$. In contrast, our most weakly coupled ensemble with $g^2 = 1$ underestimates the string tension while for $g^2 \gg 100$ the results increasingly suffer from boundary artefacts. In those ensembles, fixing the string tension at its physical value will therefore not yield dimensionful results of the expected magnitude. With this caveat in mind, we can now use a to express other dimensionful quantities in physical units (cf. Table V).

| g^2 | $\chi^{1/4} / \sigma^{1/2}$ | a [fm] | ρ [fm] | n [fm $^{-4}$] | $\chi^{1/4}$ [MeV] |
|----------|-----------------------------|-------------------|-------------------|-------------------|--------------------|
| 1 | 0.52 ± 0.057 | 0.073 ± 0.004 | 0.040 ± 0.002 | 15.69 ± 3.44 | 209.02 ± 23.04 |
| 25 | 0.29 ± 0.022 | 0.129 ± 0.002 | 0.071 ± 0.001 | 1.71 ± 0.099 | 117.61 ± 8.90 |
| 100 | 0.32 ± 0.012 | 0.142 ± 0.002 | 0.078 ± 0.001 | 1.10 ± 0.062 | 127.24 ± 5.034 |
| 1000 | 0.54 ± 0.033 | 0.219 ± 0.004 | 0.121 ± 0.002 | 0.19 ± 0.014 | 218.66 ± 13.44 |
| ∞ | 2.46 ± 0.13 | 0.205 ± 0.01 | 0.113 ± 0.006 | 0.25 ± 0.049 | 991.28 ± 51.42 |

TABLE V: Results in physical units set by the string tension $\sigma = 4.2 \text{ fm}^{-2}$.

An important dimensionful quantity is the meron-center size regulator ρ which furnishes the characteristic input scale of the dimeron ensembles (cf. Sec. II C). For $g^2 = 25 - 100$ and $\hat{\rho} = 0.55$ we find $\rho \simeq 0.07 - 0.08 \text{ fm}$, i.e. about a quarter of the typical instanton size $\bar{\rho}_I \sim 0.3 \text{ fm}$ in (singular-gauge) instanton-liquid models [23]. This indicates that our regularization procedure deforms the classical dimeron solutions only moderately and should not impede a potentially semiclassical behavior of their superpositions. The average dissociation $2 \langle |a| \rangle \sim (1 - 1.6) \rho$ of the dimerons at $g^2 = 25 - 100$ increases the effective dimeron size, on the other hand, and brings it closer to typical instanton sizes. Finally, it is useful to note that $\mu \sim \rho^{-1} \simeq 2.5 - 2.8 \text{ GeV}$ approximately sets the renormalization scale of our

ensembles. (Recall that ρ acts as an UV regulator e.g. for the action density which diverges logarithmically when $\rho \rightarrow 0$.) These μ values are of the order of typical lattice scales, which may help to explain why our results for the scale-dependent action density are compatible with lattice values.

We now turn to the dimeron density of our ensembles. Recalling the grid-point distribution from Secs. III A and III E, the four-volume of our ensemble box is given by $V_{\text{ens}} = (1.15 \times 25)^3 \times (1.15 \times 40) a^4$. The corresponding values of the dimeron density $n = (N_D + N_{\overline{D}})/V_{\text{ens}} = 487/V_{\text{ens}}$ in physical units are listed in Table V. In the preferred coupling region $g^2 = 25 - 100$ they are about 20–80% larger than the typical instanton densities $n_{I+\overline{I}} \simeq 1 \text{ fm}^{-4}$ of instanton liquid models [23]. The physical significance of this result will be discussed below. Moreover, it is interesting to note that the density $n_{M+\overline{M}} \simeq 3.2 \text{ fm}^{-4}$ of merons in the $N_M = 200$ ensemble of Ref. [14] is similar to the density of our meron constituents, i.e. approximately twice as large as our dimeron densities $n \sim 1.2 - 1.8$. This adds to our earlier evidence for an increasingly dynamical role of the largely independent meron constituents from the farthest dissociated dimerons.

It remains to put our results for the topological susceptibility in the last column of Table V into a quantitative perspective. The dimeron ensemble predictions for $\chi^{1/4}$ in the coupling region $g^2 = 25 - 100$ are about 50% smaller than the “physical” value $\chi^{1/4} = 195.03 \text{ MeV}$ (i.e. the SU(2) lattice value with the scale set by $\sigma = 4.2 \text{ fm}^{-2}$, cf. Sec. IV E). Similarly small values $\chi^{1/4} \simeq 118 - 132 \text{ MeV}$ were encountered in the meron ensembles of Ref. [14] while regular-gauge instanton ensembles yield $\chi^{1/4} \simeq 162 - 190 \text{ MeV}$. Hence our relatively small $\chi^{1/4}$ values are consistent with previous indications for the meron centers, which carry only half of the dimerons’ topological charge, to increasingly determine the topological-charge fluctuations for $g^2 \gtrsim 25$. (One should also keep in mind, however, that we consider our values for $\hat{\chi}$ as lower bounds, cf. Sec. IV E.) Another suggestive pattern in our data is the weak bare-coupling dependence of the $\chi^{1/4}$ values for $g^2 = 25 - 100$. As already alluded to, this behavior may reflect the well-known temperature independence of the topological susceptibility in the confined Yang-Mills phase [56] which in turn indicates that $\chi^{1/4}$ is relatively insensitive to temperature-induced variations of the coupling $g_{\text{YM}}^2(T)$ up to the critical temperature T_c . (For $T > T_c$, on the other hand, χ drops very rapidly.)

The unusually large value of $\chi^{1/4}$ in our $g^2 = \infty$ ensemble was already noted above in the raw data (cf. Table III). Of course this result raises suspicion. In a random distribution of merons, into which the dimerons dissociate for $g^2 \rightarrow \infty$ as far as our limited field configuration space and the boundary allows, one would expect the topological susceptibility to be an incoherent sum of single-pseudoparticle contributions and thus to have a value of the order of the pseudoparticle density. This expectation was verified explicitly in random singular-gauge instanton [23], regular-gauge instanton and single-meron [14] ensembles [85]. The fact that our for $g^2 \rightarrow \infty$ strongly increasing χ values fail to scale with the density is therefore probably another manifestation of the residual correlations between the dimerons’ meron partners and the related $g^2 \rightarrow \infty$ boundary artefacts. We recall that in Secs. IV A and IV E these artefacts were found to impede the development of a genuine random meron ensemble and to strongly contaminate the topology distributions. Fortunately, in the physically relevant coupling region $g^2 = 25 - 100$ these effects are much weaker and under far better control.

Our above results suggest a remarkably comprehensive role for dimerons in the Yang-Mills vacuum. A key feature of the emerging picture is the rather distinct division of labour between almost fully contracted, instanton-like dimerons and their far dissociated, meron-like counterparts. In dynamical equilibrium at intermediate, i.e. physical couplings both of these components coexist at fairly high densities [86]. In particular, our overall dimeron densities significantly exceed the instanton density in instanton liquid models. Hence the instanton-like dimeron component should be sufficiently populated to perform essentially all established tasks of instantons in the Yang-Mills vacuum [23, 29]. The strongly quadratic rise of our heavy-quark potentials at small interquark separations provides additional evidence in this direction (cf. Sec. IV F). The meron-like component, on the other hand, seems to be mainly responsible for the longest-distance vacuum physics including, most importantly, linear quark confinement as established in Sec. IV F and in single-meron ensembles.

On a structural level, the above reinterpretation of the instanton component in the Yang-Mills vacuum as mainly consisting of hardly dissociated dimerons is compatible with the existing instanton phenomenology as well. Indeed, due to the destructive interference between their meron-center tails the instanton-like dimerons experience much weaker long-range interactions than the almost liberated merons of the meron-like component (cf. Secs. IV B – IV D). Similar to singular-gauge instantons in sufficiently dilute superpositions they overlap less with each other, furthermore, and thus retain more of the classical solutions’ shapes and semiclassical behavior. Hence the instanton-like dimeron component indeed resembles a rather weakly interacting “liquid”. On the other hand, this raises the question why cooling studies, designed to detect semiclassical solutions in equilibrated lattice configurations, have reported clear evidence for instantons or calorons with non-trivial holonomy but none for dimerons [16, 29]. Closer inspection reveals, however, that these findings are not in conflict with our above scenario. In fact, the finite-resolution algorithms used to identify these solutions by their shapes may have counted small dimerons as instantons. Moreover, under cooling the logarithmic attraction between the dimerons’ (smoothed) meron centers can no longer be counterbalanced by their decreasing entropy. Hence the dimerons will shrink and at least partially coalesce into instantons [63] as which

they are identified afterwards.

As established in Sec. IV F, the effectively released meron centers of the meron-like dimeron component develop the strong long-range correlations required to generate confinement. Although these color correlations produce a more complex long-distance structure than encountered in fully disordered random ensembles, they still generate enough entropy for a string tension of the physically expected magnitude to develop (cf. Sec. IV F). Moreover, it seems likely that our above scenario can be extended to an at least qualitatively realistic description of the QCD vacuum. The instanton-like component of dimeron ensembles, in particular, should adapt to the presence of light quarks in essentially the same manner as in instanton liquid models. This is because most instanton effects in the light-quark sector, including the induced quark interactions which spontaneously break chiral symmetry, originate from the characteristic quark zero-modes arising in the instanton background. Since these zero modes are of topological origin, their existence and bulk properties [64] are little affected by moderate deformations of the instantons into dimerons. Hence the ensuing phenomenology should be similarly robust under such deformations.

V. SUMMARY AND CONCLUSIONS

We have studied the extent to which the Yang-Mills vacuum can be described by restricting its gauge-field content to superpositions of regularized $SU(2)$ (anti-) dimeron solutions. Our set-up and analysis of the corresponding effective theory focused mainly on structural changes in dimeron ensembles as a function of the bare gauge coupling and traced their impact on topological and confinement properties. The underlying quantum superpositions of dimerons, with their dynamics governed by the Yang-Mills action, were generated without recourse to weak-coupling or low-density approximations by Monte-Carlo simulations in a wide range of bare coupling values. The localization of the individual dimerons was enhanced by transforming them into a singular gauge, which simultaneously improves numerical efficiency, the vacuum description at shorter distances and the compatibility with semiclassically motivated instanton liquid models.

Our initial survey of dimeron ensemble properties and their coupling dependence concentrated on the spacial distribution of the dimerons, their local degree of selfduality and their meron substructure. To understand relevant aspects of the underlying inter-dimeron dynamics, we further studied short- and intermediate-range correlations between positions, topological charges and color orientations of neighboring dimerons and of their meron centers. The resulting structural patterns turned out to be multifaceted and revealing. A strong repulsion up to distances of the meron center sizes governs the short-range interactions between dimerons of both topological charges and at all couplings. In our minimally coupled and thus most ordered ensemble, we additionally find a striking (about sevenfold) preference for nearest-neighbor dimerons to carry opposite topological charges, indicating a strong intermediate-range attraction (repulsion) between dimerons of opposite (equal) topological charge. A less pronounced but still significant majority of next-to-nearest neighbors is found to carry identical topological charges. The resulting short- to mid-range order among the topological charges is reminiscent of Debye screening clouds in a plasma. These ordering patterns can be traced to the dependence of the underlying interactions on the relative color orientations between neighboring dimerons. Ensemble and configuration averages of these color orientations indicate, on the other hand, that in the mean the intermediate-range attraction between neighboring dimerons and anti-dimerons is almost completely compensated by their shorter- and longer-range repulsion and by the ensemble entropy. In any case, with increasing coupling and hence entropy the observed topological order weakens rather rapidly, together with the underlying color correlations.

The most far-reaching impact of the increasing bare coupling, however, manifests itself in the structural changes which it induces in the individual dimerons. In particular, we found the first robust evidence, established in fully interacting ensembles, for the dimerons to gradually dissociate into their meron constituents when the coupling grows. This process is driven by a competition between the coupling-dependent interactions and the entropy. Several complementary pieces of evidence further indicate that the meron constituents continuously replace the dimerons as the dynamically relevant degrees of freedom. With growing coupling the interactions between merons belonging to different dimerons therefore increasingly determine the ensemble properties. This renders the dimerons' meron partners more and more independent (except for their frozen relative color orientation) and allows our field configurations to approximate more closely those of meron ensembles. In particular, however, the changing nature of the dynamically active topological-charge carriers and of their coupling-dependent correlations leaves various revealing imprints on bulk ensemble properties.

Among the latter, the topological susceptibility is particularly relevant in our context. When calculated in a sequence of growing evaluation volumes up to the largest accessible ones, it is found to level off towards the end of the sequence. This indicates or at least foreshadows the expected saturation of the topological-charge fluctuations in the thermodynamic limit. Moreover, the resulting values of the susceptibility in the intermediate, physical coupling range remain within errors practically constant. This behavior may be related to the similarly weak temperature dependence

of the topological susceptibility in Yang-Mills theory below the deconfinement temperature. Our intermediate-coupling results reproduce those of comparable single-meron ensembles rather closely, furthermore, which seems to indicate that (on average relatively loosely bound) meron centers of dimers and single merons produce topological charge fluctuations of roughly equal strength. On the other hand, our results for the topological susceptibility underestimate lattice and instanton ensemble values by about 50%, perhaps due to insufficient saturation in our evaluation volumes and the underlying boundary effects. In any case, the dimeron ensemble predictions for the susceptibility could be straightforwardly adjusted by increasing the dimeron density.

Since the long-range color tails of less bound meron centers disorder the vacuum more strongly, we have paid particular attention to the confinement properties of the dimeron ensembles. The latter were monitored by evaluating ensemble averages of rectangular Wilson loops and by extracting the associated static quark-antiquark potentials for a wide range of coupling values. Initially, the resulting potentials are found to rise quadratically with the interquark separation. This behavior is typical for (sufficiently dilute) instanton ensembles and indicates that our short-distance potentials are dominated by contributions from moderately dissociated dimers which act essentially as singular-gauge instantons. For quark-antiquark separations beyond about half a fermi, on the other hand, the Wilson loops indeed develop an area-law behavior and the potentials consequently show the linear distance dependence characteristic of quark confinement. The associated string tension is found to grow with the coupling and to reach values of the experimentally expected order of the magnitude in the physical coupling range.

Hence we have shown – without reliance on weak-coupling or low-density approximations – that sufficiently strongly coupled and therefore on average far enough dissociated dimeron ensembles indeed produce confining long-range correlations of about the physically required strength. Since the latter originate from the meron tails of the more strongly dissociated dimers, these results also provide complementary evidence for single-meron ensembles to confine (even though our finite simulation volume and our limited field configuration space prevent the dimers from breaking up completely). Moreover, both dimeron and single-meron ensembles are found to generate confining static-quark potentials of comparable strengths at our largest accessible interquark distances. Since the linear rise of the meron-induced potential turns out to continue beyond these distances, furthermore, our above reasoning indicates that the same should happen in dimeron ensembles. Hence we expect an ongoing linear rise of the dimeron-induced potentials into the distance region where the underlying color flux tubes are fully developed.

While dimeron ensembles thus share with single-meron ensembles the main features of the confinement mechanism, they additionally provide a more complete description of the Yang-Mills vacuum. The first evidence is that our results establish how a confining meron component in the vacuum can robustly emerge from instanton and dimeron dissociation. This provides, in particular, the first quantitative confirmation for a key ingredient of the meron-induced confinement scenario envisioned more than three decades ago on the basis of qualitative arguments. In addition, our results on the coupling dependence of dimeron ensemble properties should contain useful information on their temperature dependence and, in particular, on the impact of temperature-induced variations of the gauge coupling (although we did not pursue this issue in the present paper).

Furthermore, we found evidence for the physical dimeron density to be about twice as large as typical instanton densities. This allows confining dimeron ensembles to retain a phenomenologically relevant fraction of contracted and thus more weakly interacting, “instanton-like” dimers. An independent indication for their considerable density is the strong quadratic rise of our heavy-quark potentials at short interquark distances. The instanton-like component should adapt to the presence of light quarks in essentially the same fashion as in phenomenologically successful instanton vacuum models, furthermore, since the underlying quark zero-modes in the instanton background are of topological origin and therefore little affected by the moderate deformations of instantons into contracted dimers. Hence, in addition to confining color, dimeron ensembles should be able to reproduce much of the successful vacuum and hadron phenomenology predicted by (non-confining) singular-gauge instanton ensembles.

Acknowledgments

We would like to thank E.-M. Ilgenfritz and M. Wagner for their help and numerous intense discussions, and we are grateful to M. Wagner for providing us with his pseudoparticle simulation code. H.F. and M.M.-P. acknowledge financial support from the Deutsche Forschungsgemeinschaft (DFG) under project Mu932/6-1.

-
- [1] A. Jaffe and E. Witten, *Quantum Yang-Mills Theory*, available at http://www.claymath.org/millennium/Yang-Mills_Theory/; J. Greensite, *Prog. Part. Nucl. Phys.* **51**, 1 (2003); A. Di Giacomo, arXiv:hep-lat/0510065; M. Shifman, arXiv:1007.0531; R. Alkofer and J. Greensite, *J. Phys. G: Nucl. Part. Phys.* **34** (2007) S3;
- [2] A collection of useful reviews can be found in *At the Frontier of Particle Physics – Handbook of QCD*, vol 1-4, M. Shifman (ed.), World Scientific, Singapore (2002) and *Confinement, Duality and Nonperturbative Aspects of QCD*, P. van Baal (ed.), Proc. NATO ASI Series B, vol. 368, Kluwer, New York (2002).
- [3] K. Wilson, *Phys. Rev. D* **10**, 2445 (1974); G. S. Bali, *Phys. Rep.* **343**, 1 (2001); J. Greensite, *Prog. Part. Nucl. Phys.* **51**, 1 (2003).
- [4] A. Di Giacomo, M. Maggiore, and S. Olejnik, *Nucl. Phys. B* **347**, 441 (1990); V. Singh, D. A. Browne, and R. W. Haymaker, *Phys. Lett. B* **306**, 115 (1993); G. S. Bali, C. Schlichter, and K. Schilling, *Phys. Rev. D* **51**, 5165 (1995); P. Cea and L. Cosmai, *Phys. Rev. D* **52**, 5152 (1995); M. Caselle, F. Gliozzi, U. Magnea, and S. Vinti, *Nucl. Phys. B* **460**, 397 (1996); P. Penanen, A. M. Green and C. Michael, *Phys. Rev. D* **56**, 3903 (1997); M. Zach, M. Faber, and P. Skala, *Phys. Rev. D* **57**, 123 (1998); Y. Koma, M. Koma, and P. Majumdar, *Nucl. Phys. B* **692**, 209 (2004); N.D. Hari Dass and P. Majumdar, *JHEP* **10**, 020 (2006); M. N. Chernodub and F.V. Gubarev, *Phys. Rev. D* **76**, 016003 (2007); P. Giudice, F. Gliozzi, and S. Lottini, *J. High Energy Phys.* **01** (2007) 084; R.W. Haymaker and T. Matsuki, *Phys. Rev. D* **75**, 014501 (2007); A. D’Alessandro, M. D’Elia, and L. Tagliacozzo, *Nucl. Phys. B* **774**, 168 (2007); M.S. Cardaci, P. Cea, L. Cosmai, R. Falcone and A. Papa, *Phys. Rev. D* **83**, 014502 (2011).
- [5] G.S. Bali, H. Neff, T. Düssel, T. Lippert and K. Schilling, *Phys. Rev. D* **71**, 114513 (2005); M. Pepe and U.-J. Wiese, *Phys. Rev. Lett.* **102**, 191601 (2009).
- [6] G. ’t Hooft, *Nucl. Phys. B* **138**, 1 (1978); J. Greensite, *Prog. Part. Nucl. Phys.* **51**, 1 (2003).
- [7] M. Faber, J. Greensite and S. Olejnik, *Phys. Rev. D* **57**, 2603 (1998); L. Del Debbio, M. Faber, J. Giedt, J. Greensite and S. Olejnik, *Phys. Rev. D* **58**, 094501 (1998); M. Engelhardt and H. Reinhardt, *Nucl. Phys. B* **585**, 591 (2000); M. Engelhardt, M. Quandt and H. Reinhardt, *Nucl. Phys. B* **685**, 227 (2004); S. Rafibakhsh and S. Deldar, *AIP Conf. Proc.* **892**, 527 (2007).
- [8] G. ’t Hooft, *Nucl. Phys. B* **79**, 276 (1974); A. M. Polyakov, *JETP Lett.* **20**, 194 (1974); G. ’t Hooft, in *High Energy Physics*, edited by A. Zichichi, Editrice Compositori, Bologna, (1976); S. Mandelstam, *Phys. Reports* **23C**, 245 (1976); G. ’t Hooft, *Nucl. Phys. B* **190**, 455 (1981); R. Haymaker, *Phys. Rep.* **315**, 153 (1999); A. Kronfeld, G. Schierholz and U.J. Wiese, *Nucl. Phys. B* **293**, 461 (1987); G. Ripka, *Lecture Notes in Physics* 639, Springer, Berlin (2004).
- [9] M.N. Chernodub and M.I. Polikarpov, Lectures given at *NATO Advanced Study Institute on Confinement, Duality and Nonperturbative Aspects of QCD*, Cambridge, England, 23 Jun - 4 Jul 1997, arXiv:hep-th/9710205; G. Bali, Talk given at *3rd International Conference on Quark Confinement and the Hadron Spectrum (Confinement III)*, Newport News, VA, Jun 1998, hep-ph/9809351; R. Haymaker, *Phys. Rep.* **315**, 153 (1999).
- [10] D. Tong, arXiv:hep-th/0509216; K. Konishi, *Lect. Notes Phys.* **737**, 471 (2008); D. Tong, *Annals Phys.* **324**, 30 (2009); M. Shifman and A. Yung, *Supersymmetric solitons*, Cambridge University Press, Cambridge (UK), (2009); M. Shifman, *Int. J. Mod. Phys. A* **25**, 4015 (2010).
- [11] N. Manton and P. Sutcliffe, *Topological Solitons*, Cambridge University Press, Cambridge (UK), (2004).
- [12] D. Diakonov, *Nucl. Phys. Proc. Suppl.* **195**, 5 (2009); D. Diakonov and V. Petrov, *Phys. Rev. D* **76**, 056001 (2007); D. Diakonov and N. Gromov, *Phys. Rev. D* **72**, 025003 (2005).
- [13] T.C. Kraan and P. van Baal, *Phys. Lett. B* **435**, 389 (1998); T.C. Kraan and P. van Baal, *Nucl. Phys. B* **533**, 627 (1998); K. Lee- and C. Lu, *Phys. Rev. D* **58**, 025011 (1998).
- [14] F. Lenz, J.W. Negele and M. Thies, *Ann. Phys.* **323**, 1536 (2008).
- [15] F. Bruckmann, *Eur. Phys. J. Special Topics* **152**, 61 (2007).
- [16] C. Gattringer, *Phys. Rev. D* **67** 034507 (2003); C. Gattringer and S. Schaefer, *Nucl. Phys. B* **654**, 30 (2003); E.-M. Ilgenfritz, M. Müller-Preussker, B.V. Martemyanov and A.I. Veselov, *Phys. Rev. D* **69**, 114505 (2004); E.-M. Ilgenfritz, M. Müller-Preussker and D. Peschka, *Phys. Rev. D* **71**, 116003 (2005); E.-M. Ilgenfritz, B.V. Martemyanov, M. Müller-Preussker and A.I. Veselov, *Phys. Rev. D* **71** 034505 (2005); *Phys. Rev. D* **73**, 094509 (2006).
- [17] P. Gerhold, E.-M. Ilgenfritz and M. Müller-Preussker, *Nucl. Phys. B* **760**, 1 (2007).
- [18] V. De Alfaro, S. Fubini and G. Furlan, *Phys. Lett. B* **65**, 163 (1976); *Phys. Lett. B* **72**, 203 (1977).
- [19] F. Lenz, J.W. Negele and M. Thies, *Phys. Rev. D* **69**, 074009 (2004).
- [20] M. Wagner and F. Lenz, *PoS (LAT2005)* 315; M. Wagner, *Phys. Rev. D* **75**, 016004 (2007).
- [21] A. Polyakov, *Nucl. Phys. B* **120**, 429 (1977).
- [22] I. Kogan and A. Kovner, *Monopoles, Vortices and Strings: Confinement and Deconfinement in 2 + 1 Dimensions at Weak Coupling*, in *At the frontier of Particle Physics – Handbook of QCD*, M. Shifman (ed.), World Scientific, Singapore (2001).
- [23] T. Schäfer and E.V. Shuryak, *Rev. Mod. Phys.* **70**, 323 (1998); D.I. Diakonov, *Prog. Part. Nucl. Phys.* **51**, 173 (2003). For an elementary introduction to instantons see H. Forkel, *A Primer on Instantons in QCD*, hep-ph/0009136.
- [24] C.G. Callan, R.F. Dashen and D.J. Gross, *Phys. Rev. D* **17**, 2717 (1978).
- [25] C.G. Callan, R.F. Dashen, D. J. Gross, F. Wilczek and A. Zee, *Phys. Rev. D* **18**, 4684 (1978).
- [26] D.I. Diakonov, V.Yu. Petrov and P.V. Poblitsa, *Phys. Lett. B* **226**, 372 (1989).
- [27] F. Bruckmann, S. Dinter, E.M. Ilgenfritz, M. Mueller-Preussker and M. Wagner, *Phys. Rev. D* **79**, 116007 (2009).
- [28] F. Bruckmann et al., *Phys. Rev. D* **85**, 034502 (2012).
- [29] E.-M. Ilgenfritz, M.L. Laursen, G. Schierholz, M. Müller-Preussker, H. Schiller, *Nucl. Phys. B* **268**, 693 (1986); M.-C.

- Chu and S. Huang, Phys. Rev. D **45**, 2446 (1992); M.-C. Chu, J.M. Grandy, S. Huang and J. Negele, Phys. Rev. D **49**, 6039 (1993); A. Hasenfratz, T. DeGrand, and D. Zhu, Nucl. Phys. **B 478**, 349 (1996); P. de Forcrand, M. G. Perez, I.-O. Stamatescu, Nucl. Phys. **B 499**, 409 (1997); D.A. Smith and M.J. Teper, Phys. Rev. D **58**, 014505 (1998); P. van Baal, Nucl. Phys. Proc. Suppl. **63**, 126 (1998); A. Hasenfratz and C. Nieter, Nucl. Phys. Proc. Suppl. **73**, 503 (1999); M.G. Perez, O. Philipsen, I.-O. Stamatescu, Nucl. Phys. **B 551**, 293 (1999); T. DeGrand, A. Hasenfratz, Phys. Rev. D **64**, 034512 (2001); E.-M. Ilgenfritz et al, Nucl. Phys. Proc. Suppl. **119**, 754 (2003); C. Gattringer et al., Nucl. Phys. Proc. Suppl. **129**, 653 (2004), F. Bruckmann et al., Contribution to Lattice 2004, Batavia, Illinois (2004), hep-lat/0408036.
- [30] C.G. Callan, R.F. Dashen and D. J. Gross, Phys. Lett. **B66**, 375 (1977).
- [31] C.G. Callan, R.F. Dashen and D. J. Gross, Phys. Rev. D **19**, 1826 (1979).
- [32] M. Faber, H. Markum, S. Olejnik and W. Sakuler, Nucl. Phys. B (Proc. Suppl.) **42**, 487 (1995).
- [33] N. Drukker, D.J. Gross and N. Itzhaki, Phys. Rev. D **62**, 086007 (2000); J.V. Steele and J.W. Negele, Phys. Rev. Lett. **85**, 4207 (2000); H. Reinhardt and T. Tok, Phys. Lett. **B 505**, 131 (2001); A. Montero and J.W. Negele, Phys. Lett. **B 533**, 322 (2002); K. Kondo, N. Fukui, A. Shibata and T. Shinohara, Phys. Rev. D **78**, 065033 (2008).
- [34] J. Glimm and A. Jaffe, Phys. Rev. Lett. **40**, 277 (1978); Phys. Rev. D **18**, 463 (1978).
- [35] S. Coleman, *The uses of instantons*, in *The Ways of Subnuclear Physics*, Ed. A. Zichichi (Plenum, New York, 1977).
- [36] V.L. Berezinsky, Sov. Phys. JETP **34**, 610 (1972); J. Kosterlitz and D. Thouless, J. Phys. **C6**, 1181 (1973).
- [37] C.G. Callan, R. Dashen and D. Gross, Phys. Lett. **B 65**, 375 (1977).
- [38] See for example H. Reinhardt, Nucl. Phys. **B 628**, 133 (2002).
- [39] G. 't Hooft, Phys. Rev. D **14**, 3432 (1976).
- [40] B. Gidas, J. Math. Phys. **20**, 2097 (1979).
- [41] A.A. Belavin, A.M. Polyakov, A.S. Schwartz, and Yu.S. Tyupkin, Phys. Lett. **B59**, 85 (1975).
- [42] A. Vainsthein et al, *ABC of Instantons*, in *ITEP Lectures on Particle Physics and Field Theory* (World Scientific, Singapore, 1999).
- [43] C.G. Callan, R. Dashen and D. Gross, Phys. Lett. **B 77**, 270 (1978).
- [44] A. Ringwald and F. Schrempp, Phys. Lett. **B 459**, 249 (1999).
- [45] Ph. de Forcrand and M. Pepe, Nucl. Phys. **B 598**, 557 (2001); Ph. de Forcrand and M. Pepe, Nucl. Phys. **B (Proc. Suppl.) 94**, 498 (2001); F. Gutbrod, Eur. Phys. J. C **8**, 1 (2001); Nucl. Phys. **B 720**, 116 (2005).
- [46] D.I. Diakonov and V. Petrov, Nucl. Phys. **B 245**, 259 (1984).
- [47] M.-C. Chu, S. M. Ouellette, S. Schramm and R. Seki, Phys. Rev. D **62**, 94508 (2000); A. Hasenfratz, Phys. Lett. **B 476**, 188 (2000).
- [48] N.J. Dowrick and N.A. McDougall, Phys. Lett. **B 285**, 269 (1992); S. Samuel, Mod. Phys. Lett. A **7**, 2007 (1992); H. Kikuchi and J. Wudka, Phys. Lett. **B 284**, 111 (1992).
- [49] H. Forkel, Phys. Rev. D **71**, 054008 (2005).
- [50] E.V. Shuryak and J.J.M. Verbaarschot, Phys. Rev. D **52**, 295 (1995); H. Forkel, Braz. J. Phys. **34**, 875 (2004); *QCD glueball sum rules and vacuum topology*, Proceedings of “Continuous advances in QCD,” Minneapolis, 2006, p. 283, World Scientific, Singapore (2007), arXiv:hep-ph/0608071.
- [51] E. Witten, Nucl. Phys. **B 156**, 269 (1979); G. Veneziano, Nucl. Phys. **B 159**, 213 (1979).
- [52] E. Seiler, I.O. Stamatescu, MPI-PAE/PTh 10/87; E. Seiler, Phys. Lett. **B 525**, 355 (2002); M. Lüscher, Phys. Lett. **B 593**, 296 (2004).
- [53] A.S. Kronfeld, M.L. Laursen, G. Schierholz, and U.-J. Wiese, Nucl. Phys. **B 292**, 330 (1987); A.S. Kronfeld, M.L. Laursen, G. Schierholz, C. Schliefermayer and U.-J. Wiese, Nucl. Phys. **B 305**, 661 (1988); T.A. deGrand and A. Hasenfratz, Nucl. Phys. **B 520**, 301 (1998); E. Vicari and H. Panagopoulos, Phys. Rep. **470**, 93 (2009).
- [54] B. Lucini and M. Teper, JHEP **06**, 050 (2001).
- [55] M. Teper, Nucl. Phys. B (Proc. Suppl.) **109A**, 134 (2002); L. Del Debbio, H. Panagopoulos and E. Vicari, JHEP **0208**, 044 (2002).
- [56] B. Allés, M. D’Elia and A. Di Giacomo, Nucl. Phys. **B 494**, 281 (1997) [Erratum ibid. **B 679** (2004) 397]; C. Gattringer, R. Hoffmann and S. Schaefer, Phys. Lett. **B 535**, 358 (2002); B. Lucini, M. Teper and U. Wenger, arXiv:hep-lat/0401028.
- [57] K. Dietz and T. Filk, Phys. Rev. D **27**, 2944 (1983).
- [58] F. V. Gubarev, L. Stodolsky and V. I. Zakharov, Phys. Rev. Lett. **86**, 2220 (2001).
- [59] R. Akhoury and V.I. Zakharov, Phys. Lett. **B 438**, 165 (1998) [arXiv:hep-ph/9710487]; K.G. Chetyrkin, S. Narison and V.I. Zakharov, Nucl. Phys. **B 550**, 353 (1999); V.I. Zakharov, Nucl. Phys. B (Proc. Suppl.) **164**, 240 (2007).
- [60] M. Campostrini, A. Di Giacomo and G. Paffuti, Z. Phys. C **22**, 143 (1984).
- [61] I. Halperin and A. Zhitnitsky, Mod. Phys. Lett. A **13**, 1955 (1998).
- [62] H. Forkel, Phys. Rev. D **73**, 105002 (2006); Int. J. Mod. Phys. E **16**, 2789 (2007); Phys. Rev. D **81**, 085030 (2010); PoS (QCD-TNT-II) 022, arXiv:1112.5476 [hep-ph].
- [63] J.V. Steele and J.W. Negele, Phys. Rev. Lett. **85**, 4207 (2000).
- [64] J. Kiskis, Phys. Rev. D **18**, 3690 (1978).
- [65] One may abandon the requirement that the constituent fields are Yang-Mills solutions, e.g. by multiplying them with variable coefficients [20]. The latter approach leads to a more flexible vacuum description but prevents a semiclassical interpretation.
- [66] In the words of Sidney Coleman [35]: “I can see nothing wrong with this idea in principle, but the details of the argument involve a stupendous amount of hand-waving. This part is just a suggestion (although a very clever suggestion) that may or may not someday become a theory of confinement.”
- [67] The dimeron’s entropy is the logarithm of its collective-coordinate (or moduli) space volume.

- [68] As in several lower-dimensional systems, in the thermodynamic limit the dimeron dissociation process may therefore lead to a sharp transition of Kosterlitz-Thouless type [36, 37] from a deconfining to a confining phase.
- [69] i.e. the 2nd Chern class of the associated principal fiber bundle
- [70] More generally, these are the $N_c^2 - 1$ “Euler angles” which parametrize (constant) $SU(N_c)$ group elements.
- [71] It may be useful to recall that the superposition of singular-gauge dimerons is *not* gauge-equivalent to a superposition of regular-gauge dimerons.
- [72] From the practical point of view this is fortunate since no multi-meron solutions with $|Q| > 1$ seem to be known analytically.
- [73] More precisely, all four coefficients of the quaternion representation (11) are varied independently. The constraint among them is reinstated only afterwards by rescaling all coefficients with a common factor. (Hence $d\mu(c_i)$ represents the Haar measure on $SU(2) \sim S^3$.)
- [74] The singular-gauge induced singularities are so strongly localized (even after regularization, cf. Sec. II C), on the other hand, that they have practically no impact on the simulations.
- [75] In practice, these densities were calculated by dividing the box volume into 60 concentric, spherical shells around the reference pseudoparticle, counting the number of either equally or oppositely charged pseudoparticle centers contained in it, and dividing by the shell volume V_{shell} . The latter is calculated analytically as long as the shells lie fully inside the ensemble volume (cf. Sec. III A), and otherwise as $V_{\text{shell}} = V N_{\text{shell}}/N_V$ where N_V points are randomly distributed over the ensemble box and N_{shell} is the number of them which fall into the shell.
- [76] This screening behavior should not be confused with the light-quark and anomaly-induced topological charge screening in the QCD vacuum [47], with its strong impact on η' meson [48] and pseudoscalar glueball properties [49, 50].
- [77] In order to reduce the impact of boundary effects we include only those (anti-)dimerons whose centers lie inside a (hyper)sphere of radius one around the mid point of the box. The inter-meron separation $2\langle|a|\rangle$ of the dimerons then restricts the maximal distance of the meron center from the box center to $1 + \langle|a|\rangle$, i.e. on average meron centers lie maximally a distance $\langle|a|\rangle$ outside the ball. For $g^2 = 1$, where the boundary effects are strongest, the smallest $\langle|a|\rangle \sim 0.27$ then reduces their impact by ensuring that the meron centers remain closest to the sphere. For the maximal couplings, on the other hand, one finds $\langle|a|\rangle \sim 3/2$.
- [78] Even for $N_D = N_D^{\text{strict}}$ strict CP invariance would hold only in the infinite-volume limit and/or with infinite ensemble statistics, incidentally, since the topological charge density of the dimerons is not fully contained in our evaluation volumes. However, this boundary artefact is mitigated already in relatively small volumes by the short-range anticorrelations among the dimerons’ topological charges (cf. Sec. IV B).
- [79] Our V resolution is obtained by using volumes with extent 1.2 and step size 0.1 in the three spacial directions, and a step width of 0.03 in the temporal direction which maximally extends to 4.0.
- [80] The values of very small Wilson loops could alternatively be obtained analytically since our gauge field configurations (13) become constant at length scales $\ll \rho$ (cf. Ref. [14]).
- [81] The statistical error of the data points from the subvolumina is somewhat smaller than that from their central hyperplanes. When plotting $\langle W[C(R, 2R)] \rangle$ as a function of R , incidentally, some seemingly correlated discrepancies between these data sets become nevertheless visible for $g^2 = 1$ but not for larger couplings. Hence these distortions may indeed originate from boundary effects (cf. Sec. III D) and appear to be sufficiently suppressed in the chosen subvolumina.
- [82] Linear short-distance contributions to the static quark potential (originating e.g. from a nonlocal two-dimensional gluon condensate [58] and modeled by a tachyonic UV gluon mass) were argued for as well [59]. (It is conceivable that the latter may also contribute in dimeron ensembles where the linear behavior of $V(R)$ sets in at rather small distances.)
- [83] In Refs. [14, 19] it was argued that the meron peak contributions, which diverge logarithmically for $\rho \rightarrow 0$, should be subtracted from $\langle s \rangle$ in meron ensembles. The remaining, about 25-35% reduced “background” action density is then considered as the physical result, renormalized at ρ^{-1} . For our more localized singular-gauge dimerons this procedure will be less effective, and we shall not attempt to implement it here.
- [84] The relation given in Ref. [23] contains an error. We thank Thomas Schäfer for clarifying correspondence on this issue.
- [85] Even at finite coupling, correlations between instantons are known to be fairly weak in pure Yang-Mills theory and in singular-gauge instanton ensembles (without light quarks). Hence the topological susceptibility can be used to estimate the instanton density in the Yang-Mills vacuum [23].
- [86] Indications for the coexistence of instantons and merons at comparable densities in the Yang-Mills vacuum were also found in a variational approach [62].

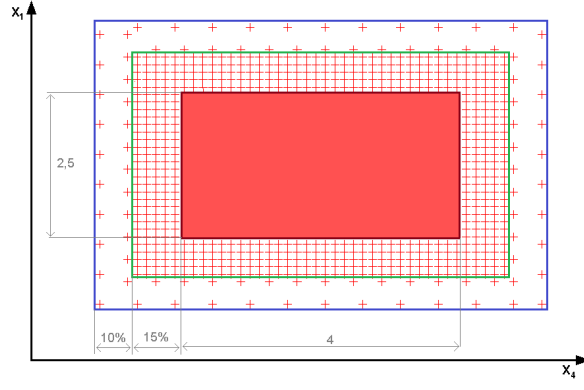


FIG. 1: The multi-layered multigrid designed to control boundary effects when numerically evaluating the action density.

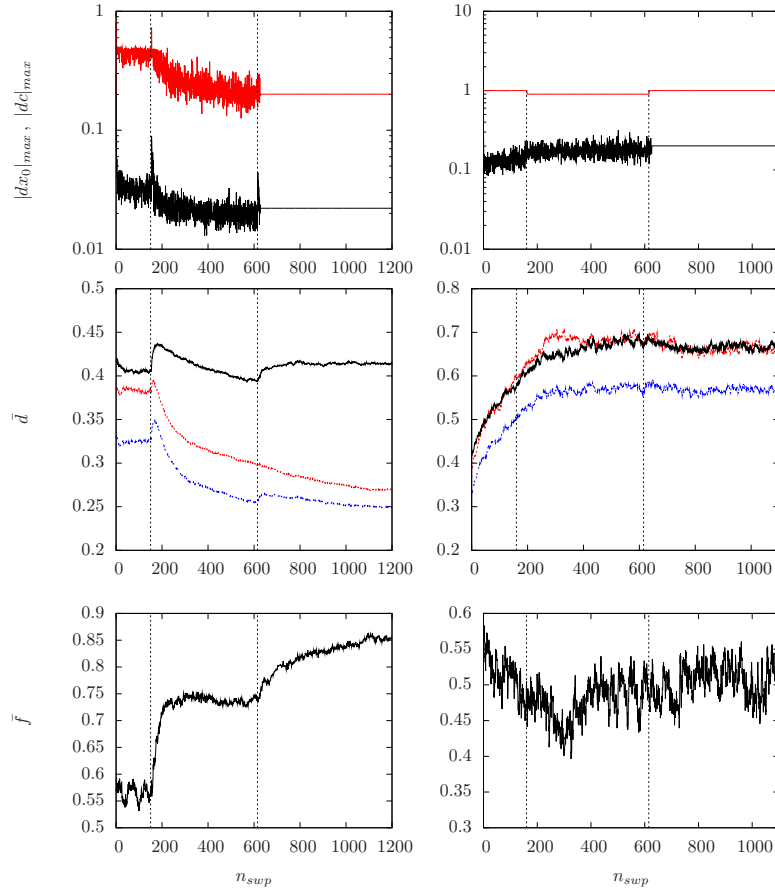


FIG. 2: The thermalization histories of simulations with $g^2 = 1$ (left panels) and $g^2 = 25$ (right panels) as a function of the number n_{swp} of sweeps. The uppermost row shows the evolution of the maximal step widths in position (lower, black curves) and color (upper, red curves) space. In the second row we plot the average distances \bar{d} between nearest-neighbor dimers of equal (black curves, uppermost for $g^2 = 1$), opposite (red curves, intermediate for $g^2 = 1$) and arbitrary (lowest-lying, blue curves) topological charge. The last row shows the average probability \bar{f} for the nearest neighbor of a given meron center to have opposite topological charge. (The dotted vertical lines indicate the sweep numbers at which the resolution of the action sampling is increased. For a stringent test of the resolution quality we enhance the corresponding action changes by smearing the meron-center singularities less broadly, corresponding to $\rho^2 = 0.2$, in the $g^2 = 1$ simulation (left panels). For $g^2 = 25$ (right panels) we use our standard value $\rho^2 = 0.3$.)

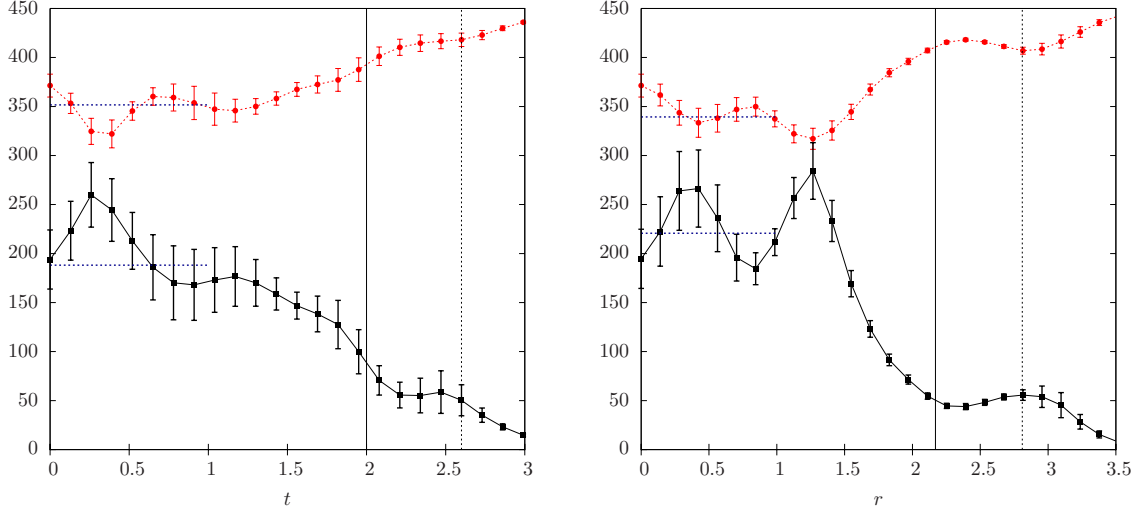


FIG. 3: The averaged action density $\langle s \rangle$ (black squares, full line) and quadratic “plaquette” Wilson loop expectation values $\langle W \rangle$ (red circles, dotted line, multiplied by 450) along the time direction (left panel) and along the spatial diagonals (right panel) from the center of the simulation box for $g^2 = 1$. (The dashed horizontal lines are fits to constant plateaus for $t, r \leq 1$. The two vertical lines indicate the boundaries of the core and sampling volumes.)

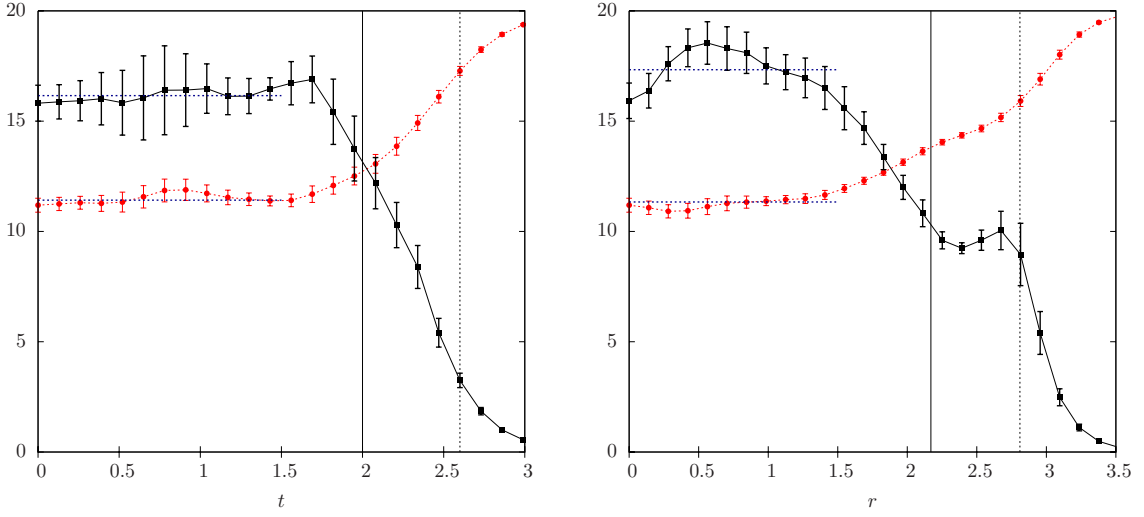


FIG. 4: Same as in Fig. 3, but for $g^2 = 25$ (and with $\langle W \rangle$ multiplied by 20).

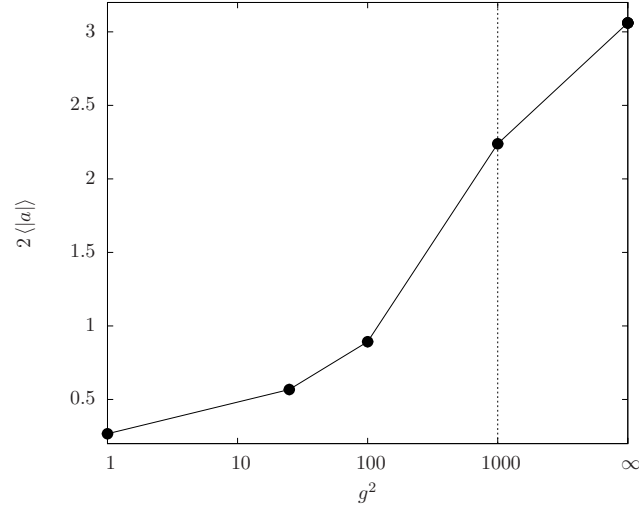


FIG. 5: The average separation $2\langle|a|\rangle$ between the (anti-) meron centers of the (anti-) dimers as a function of the squared gauge coupling. (The error bars are smaller than the plot symbols and the dotted vertical line indicates the scale change at $g^2 = 1000$.)

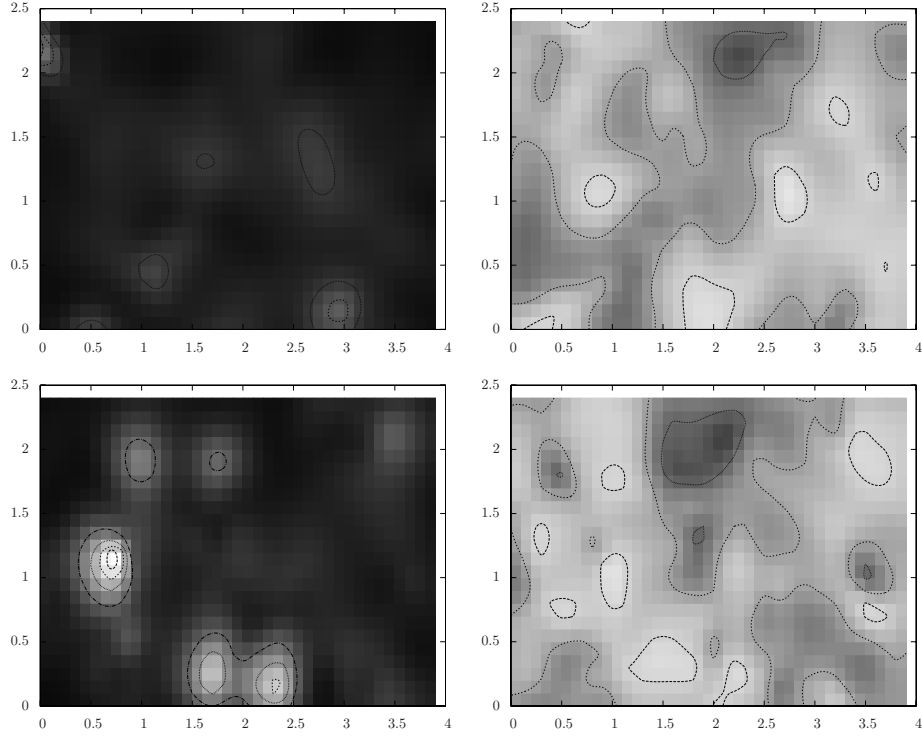


FIG. 6: The action (left panels) and selfduality (right panels) densities of a typical $g^2 = 1$ ensemble configuration in two cross sections parallel to the $x_1 - x_4$ plane. Lighter shades of gray indicate larger values. The ordinates denote the x_1 and the abscissas the x_4 direction. The upper row shows the densities in the hyperplane at $(x_2, x_3) = (0.4, 0.4)$ and the lower row those in the plane at $(x_2, x_3) = (0.4, 1.2)$.

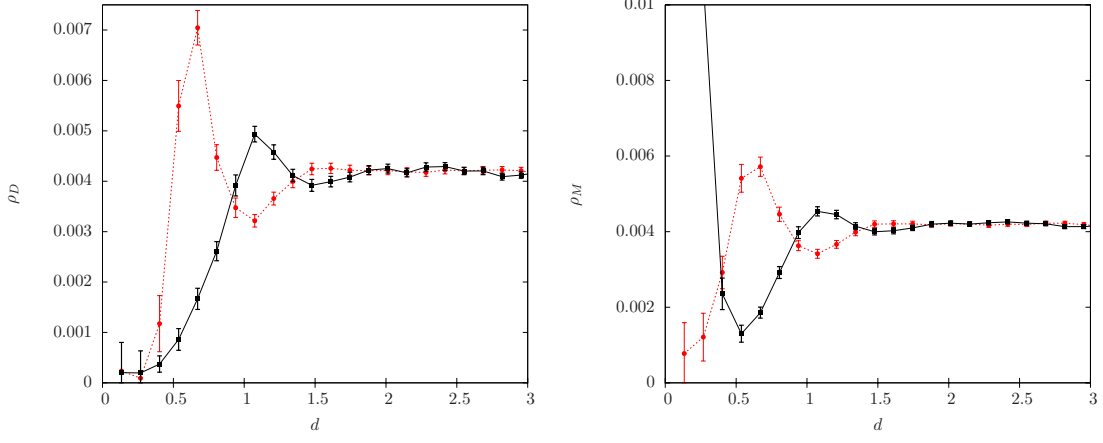


FIG. 7: The average radial density of topologically equally (black squares, full line) and oppositely (red bullets, dotted line) charged dimers ρ_D (left panel) and merons ρ_M (right panel) as a function of the distance from a fixed (anti-) (di)meron at $g^2 = 1$.

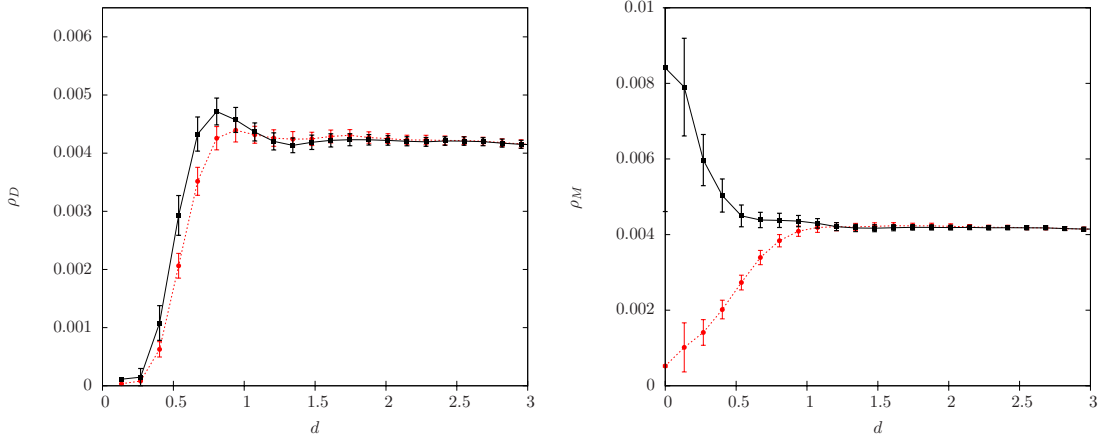


FIG. 8: The same as in Fig. 7, but for $g^2 = 25$.

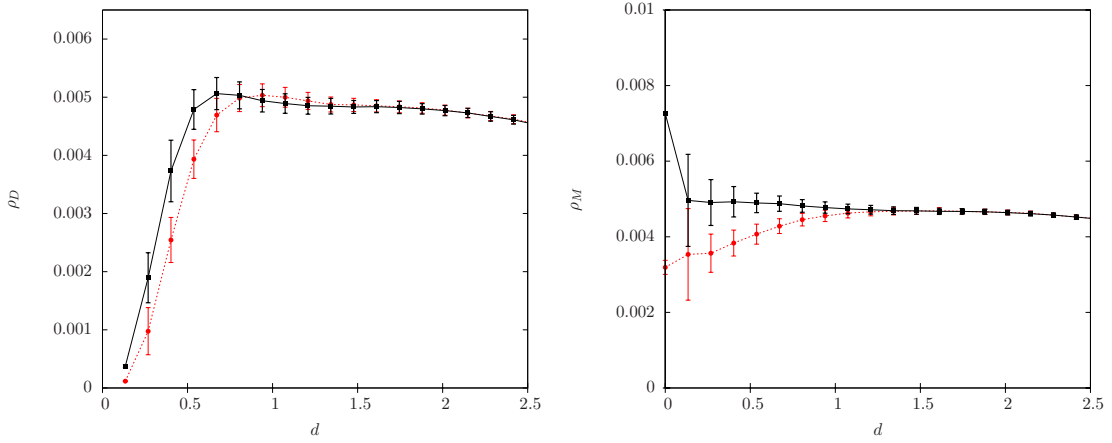


FIG. 9: The same as in Fig. 7, but for $g^2 = 100$.

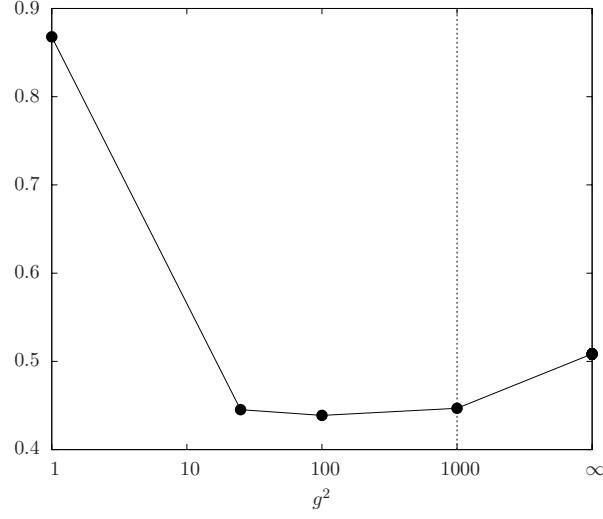


FIG. 10: The average probability $\langle f_{D\bar{D}} \rangle$ for the nearest neighbor of a dimeron to have opposite topological charge. (The error bars are smaller than the plot symbols and the dotted vertical line indicates the scale change at $g^2 = 1000$.)

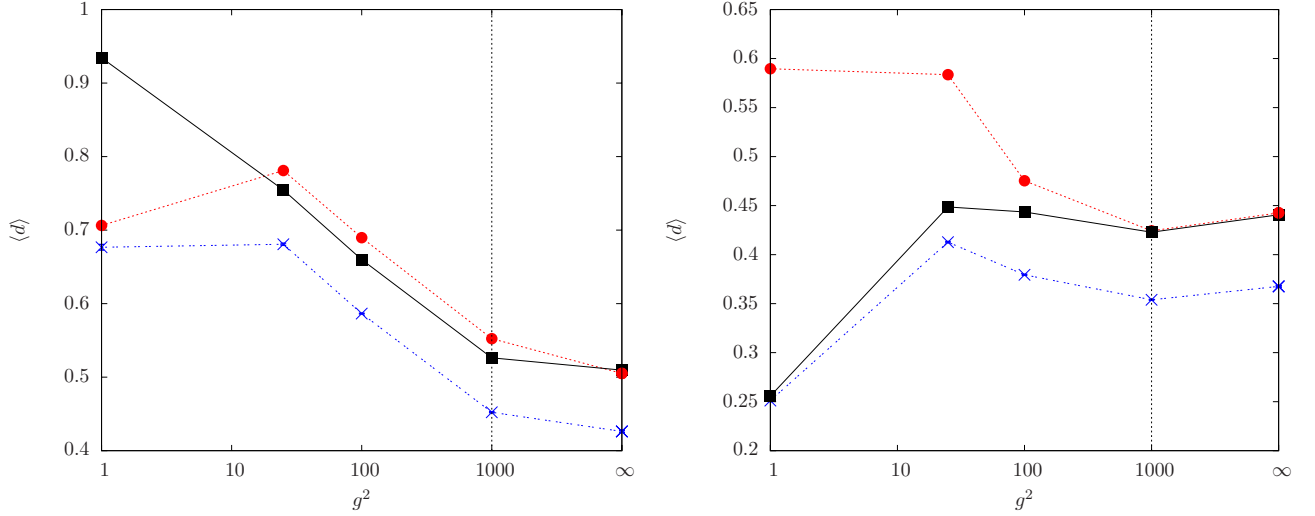


FIG. 11: The left panel shows the average distance $\langle d \rangle$ of a reference dimeron center from its nearest neighbor with equal (black squares, full line) and opposite (red bullets, dotted line) topological charge Q . The nearest-neighbor distance $\langle d \rangle$ independent of Q is also included (blue crosses, dashed line). The right panel shows the same curves for the average distances between meron instead of dimeron centers. (The error bars are smaller than the plot symbols and the dotted vertical line indicates the scale change at $g^2 = 1000$.)

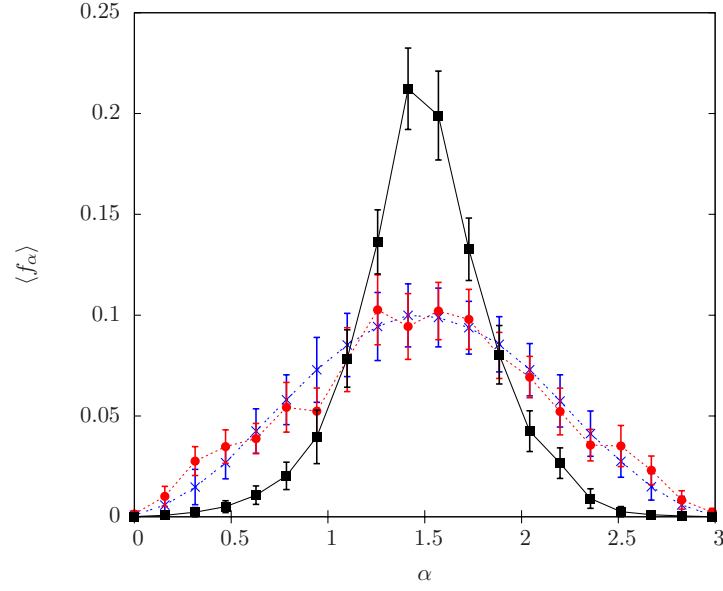


FIG. 12: The distribution of the average color angle $\langle \alpha \rangle$ between nearest neighbor pseudoparticles of equal (black squares, full line) and opposite (red bullets, dotted line) topological charge at $g^2 = 1$. For comparison, we also show $\langle \alpha \rangle$ for a random pseudoparticle distribution (i.e. at $g^2 = \infty$; blue crosses, dashed line) which is independent of the relative topological charge of the neighbors. (The error bars indicate the statistical standard deviation of the averages per bin.)

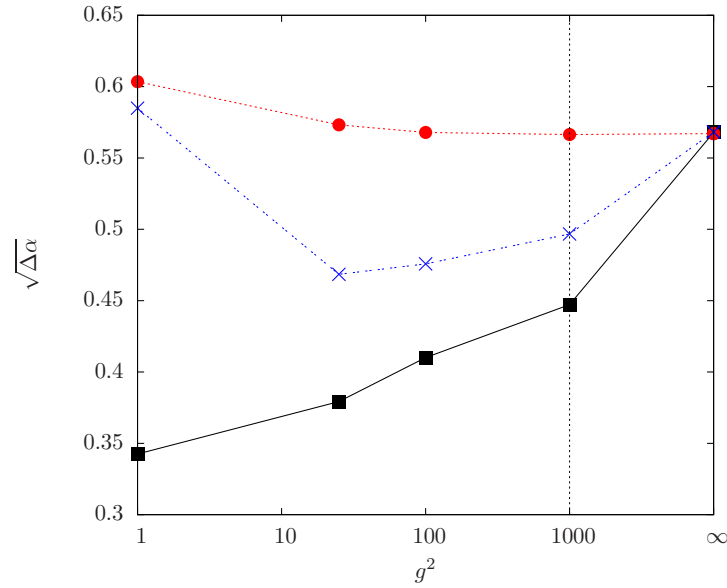


FIG. 13: The standard deviation of the $\langle \alpha \rangle$ distribution between nearest neighbors of equal (black squares, full line) and opposite (red bullets, dotted line) topological charge Q as a function of g^2 . The standard deviation of the color orientation for nearest neighbors independent of Q is also included (blue crosses, dashed line).

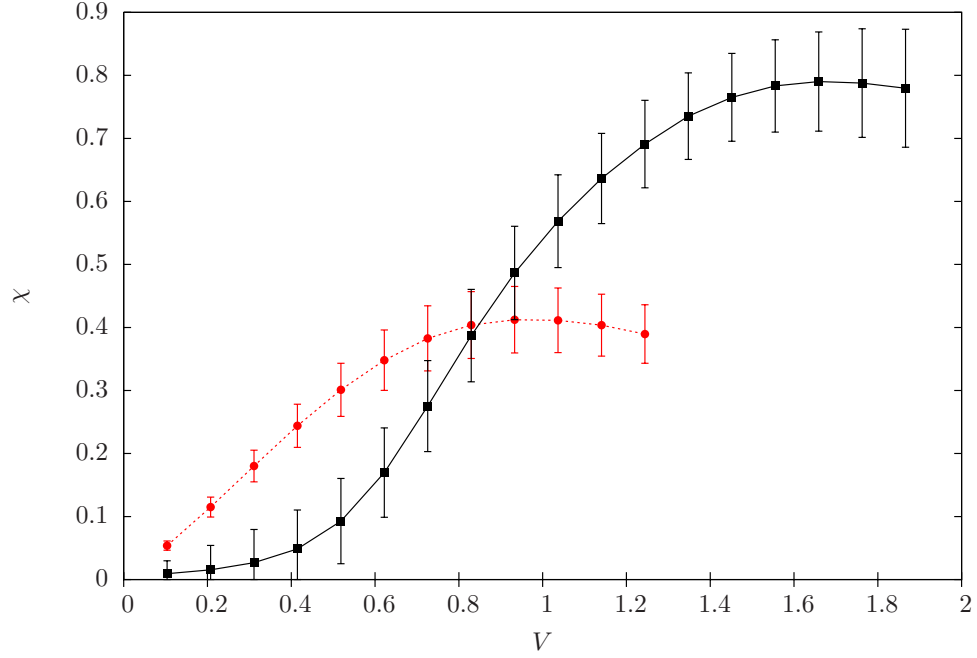


FIG. 14: The topological susceptibility χ as a function of the spacetime volume V for $g^2 = 1$ (red bullets, dotted line) and $g^2 = 100$ (black squares, full line).

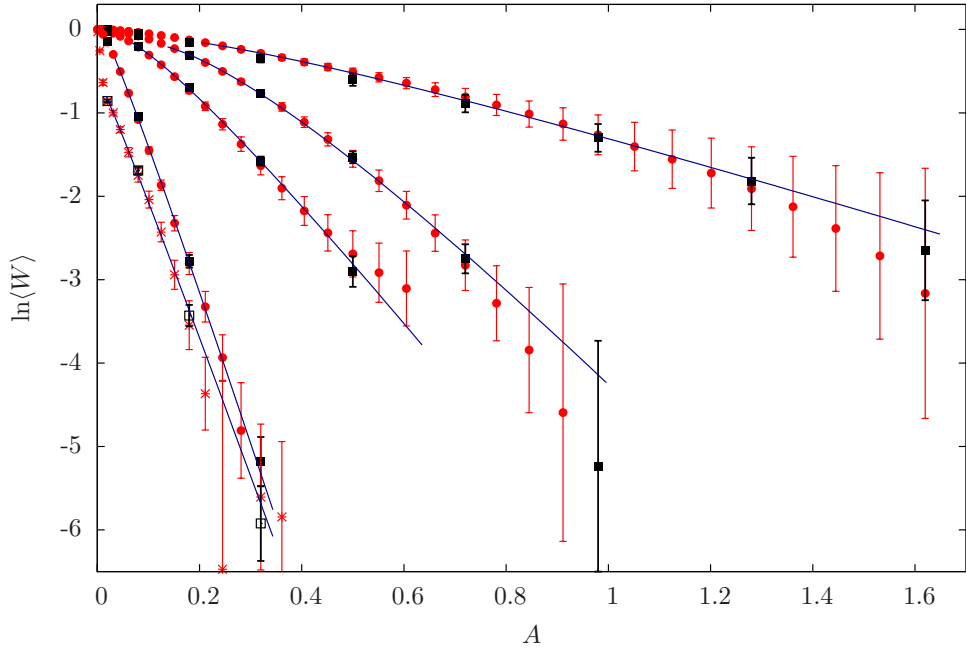


FIG. 15: The logarithm of the expectation value of rectangular Wilson loops with area A (and side length $R = T/2 = \sqrt{A/2}$) for the square coupling values $g^2 = 1, 25, 100, 1000$ and ∞ . (For increasing coupling the data lie below each other.) The black squares (boxes) are obtained from the loops in the full evaluation volume, the red dots (asterisks) from the loops in the central hyperplanes. The fit curves to $f(A)$, as described in the text, are drawn as full lines in their fit intervals.

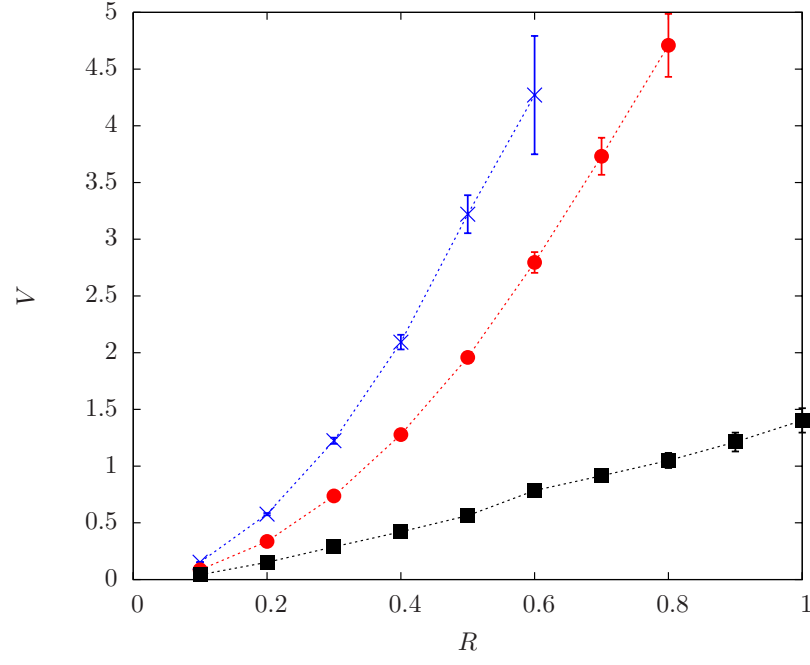


FIG. 16: The heavy-quark potentials $V(R)$ for the square coupling values $g^2 = 1, 25$ and 100 . (The stronger potentials correspond to larger couplings.)

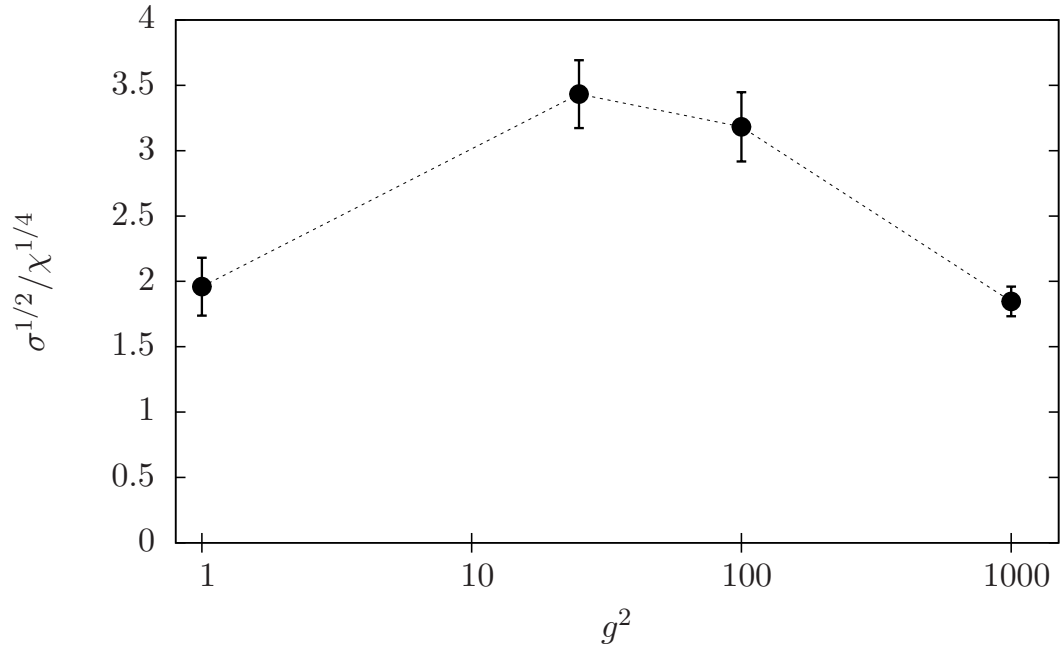


FIG. 17: The dimensionless ratio $\sigma^{1/2}/\chi^{1/4}$ as a function of the square coupling g^2 .